BRNO UNIVERSITY OF TECHNOLOGY

VYSOKÉ UČENÍ TECHNICKÉ V BRNĚ

FACULTY OF MECHANICAL ENGINEERING

FAKULTA STROJNÍHO INŽENÝRSTVÍ

INSTITUTE OF PHYSICAL ENGINEERING

ÚSTAV FYZIKÁLNÍHO INŽENÝRSTVÍ

DYNAMICS OF MICROPARTICLES OPTICALLY TRAPPED IN VACUUM

DYNAMIKA MIKROČÁSTIC ZACHYCENÝCH V OPTICKÉ PASTI VE VAKUU

SHORT VERSION OF DOCTORAL THESIS

TEZE DIZERTAČNÍ PRÁCE

AUTHOR
AUTOR PRÁCE

Mgr. Vojtěch Svak

SUPERVISOR
ŠKOLITEL

Mgr. Oto Brzobohatý, Ph.D.

BRNO 2021

ABSTRACT

A microparticle levitating in vacuum only by optical forces constitutes a mechanical system which is extremely well isolated from its environment, including its sources of noise. This unique feature provides the system with outstanding sensitivity on any change of surrounding conditions. We introduce a unique experimental set-up for trapping in vacuum which we built the Institute of scientific instruments of CAS in Brno. Subsequently we provide an experimental study of mechanical effect of circularly polarized light which, contrary to linearly polarized light, generates non-conservative contribution to the optical force field. We follow by presenting observation of optical binding of two particles in free space in vacuum which has never been realised before and show how the inter-particle interaction can be tuned and characterized. In the end we introduce a promissing method for optical force field estimation based on particles stochastic trajectory analysis.

KEYWORDS

optical trapping, optical levitation, counter-propagating beams, laser induced desorption, optical catapult, optical spin, non-conservative force, optical binding, force field estimation

ABSTRAKT

Mikročástice levitující ve vakuu pouze za pomoci silových účinků světla představuje mechanický systém, který je extrémně dobře izolován od okolních a jeho zdrojů šumu. Tato unikátní vlastnost poskytuje tomuto systému nevídanou citlivost na změny okolních podmínek. V předkládané práci je popsáno technické řešení experimentální sestavy pro optické chytání ve vakuu, která byla realizována v laboratořích skupiny levitační fotoniky Ústavu přístrojové techniky AVČR v Brně. Dále je prezentována experimentální studie dynamiky částice zachycené v kruhově polarizovaném optickém poli, které generuje nekonzervativní složku pole optické síly. Následuje experimentální pozorování a popis dynamiky dvou opticky vázaných mikročástic ve volném prostoru ve vakuu, což je konfigurace, která nebyla nikdy předtím realizována. Závěrem je představena zcela originální metoda pro odhad silového pole optické pasti založená na analýze stochastické trajektorie zachycené částice.

KLÍČOVÁ SLOVA

optické chytání, optická levitace, protiběžné svazky, laserem indukovaná desorpce, optický katapult, optický spin, nekonzervativní síla, optická vazba, odhad silového pole

SVAK, Vojtěch. *Dynamics of microparticles optically trapped in vacuum*. Brno, 2021, 58 p. Doctoral thesis. Brno University of Technology, Faculty of Mechanical Engineering, Institute of Physical Engineering. Advised by Mgr. Oto Brzobohatý, Ph.D.

DECLARATION

I declare that I have written the Doctoral Thesis titled "Dynamics of microparticles optically trapped in vacuum" independently, under the guidance of the advisor and using exclusively the technical references and other sources of information cited in the thesis and listed in the comprehensive bibliography at the end of the thesis.

As the author I furthermore declare that, with respect to the creation of this Doctoral Thesis, I have not infringed any copyright or violated anyone's personal and/or ownership rights. In this context, I am fully aware of the consequences of breaking Regulation § 11 of the Copyright Act No. 121/2000 Coll. of the Czech Republic, as amended, and of any breach of rights related to intellectual property or introduced within amendments to relevant Acts such as the Intellectual Property Act or the Criminal Code, Act No. 40/2009 Coll., Section 2, Head VI, Part 4.

Brno ....

author's signature

ACKNOWLEDGEMENT

I thank my supervisor, Oto Brzobohatý, for his guidance and patience during my studies. He was always there to share his experience and his endless positivity. I thank prof. Pavel Zemánek, who is the most supportive chief. I also thank Stephen Simpson, who was an inexhaustible well of inspiring ideas and who patiently corrected my English and mz math every time I asked him. Finally I thank all Microphotonics team members for their open and helpful attitude.

The research was supported by the Centre of Excellence for Classical and Quantum Interactions in Nanoworld (GB14-36681G) and ALISI - Centre of Advanced Diagnostic Methods and Technologies (LO1212).

Brno . . . .

author's signature

Contents

1 Introduction

In 1970, Arthur Ashkin published seminal paper showing that it is possible to accelerate and grab micron-sized transparent particles by focused laser beam [1]. Since then, the field of optical micro-manipulation underwent vast development [2]. Optical trapping techniques played important role in research across physical, chemical and biological sciences with applications starting at manipulation with atoms and micro-particles leading to manipulation of living cells [3] or such demanding experiments as measurement of tiny forces between single molecules in various molecular motors [4, 5].

The mostly used optical tool, *optical tweezers* [6], is created by a laser beam tightly focused by a high numerical aperture microscope objective. Such tool, referred to as an optical trap, is capable of trapping and manipulating a single object of size ranging from tens of nanometers to tens of micrometers. Trapping several such objects can be achieved by splitting the original laser beam into several beams by phase grating generated by spatial light modulator (SLM) [7] or by amplitude grating generated by digital micro mirror device (DMD), obtaining so called *holographic optical tweezers*. Another approach to create multiple traps is *time-sharing trapping* [8], where the trapping laser beam is being switched between individual traps so fast that the particles do not have enough time to escape due to Brownian motion. Such speeds are achieved using galvano-optical mirrors or acousto-optic deflectors (AODs). Holographic optical tweezers is the most flexible and all-purpose method for trapping several tens of objects enabling to trap in 3D and even to shape the trapping potential of individual trap. The universality is counterbalanced by several limiting factors, mainly by low trapping efficiency and slow modification of the trapping potential (tens of Hz) compared to time-sharing.

Extensive systems of optical traps can be fabricated by an interference of several laser beams, when each local intensity maximum/minimum constitutes a possible optical trap. Possibility of creating two-dimensional structures of traps on surface via interference field of co-propagating beams was reported [9, 10, 11]. Three-dimensional structure of traps was realised in the standing wave formed by interference of two counter-propagating beams [12, 13, 14, 15]. Notably the magnitude and even the direction of force acting on a particle placed in such structure is very sensitive on the particle size which is elegantly exploited in various techniques of *optical sorting* [16, 17, 18].

All of the experiments listed above manipulates with objects in liquid. Liquid media strongly damp the motion of trapped objects to become overdamped, and the particle inertia does not play any role in observed particle dynamics. Such damping improves the trap stability and makes trapping in liquid relatively straight-

forward. In contrast, trapping particles in low viscosity environment (e.g. air, low pressure) is more challenging, because mechanical noise of the set-up or relative intensity noise of the trapping laser affect the trapping stability. In his pioneering experiments regarding trapping in air [19], A. Ashkin used inverted geometry of optical tweezers [20, 21, 22]. Here, the gravitational force acting on the particle is compensated by radiation pressure of the upward propagating trapping beam. Such a geometry was used for investigation of properties of dust particles, for example size, composition, morphology and phase [23, 24, 25]. Another geometry, which does not employ external force for particle containment, uses two counter-propagating Gaussian beams. It was used for trapping of solid airborne particles [26, 27], study of ice formation [28], for trapping of salt and sugar crystal from solution [29] and for study of optical interaction between several oil droplets in the air [30].

Single particle held in an optical trap behaves as a mechanical oscillator. If it is placed in vacuum, it becomes isolated from the external environment possible which results in very low mechanical damping and high mechanical quality factors of such oscillator. This unique property attracted a lot of attention during the last decades. Researchers thoroughly studied the center-of-mass (CoM) motion of particle trapped in various trap geometries and showed methods how to control it [31, 32, 33]. Extracting energy from the CoM mode and reaching quantum ground state has become one of the main challenges in the field. This so-called *cooling* was successfully implemented [34, 35]. Quantum ground sate cooling was reported using already two techniques, the first one being the passive technique using coherent scattering into an optical resonator [36], the second one used active feedback cooling [37]. Further more, librational motion [38], rotation [39, 40] and nonlinear dynamics [41, 42] of this optomechanical system are started to be examined in detail. The ultimate goal of all these studies is to engineer a platform suitable for studying the border between classical and quantum mechanics [43, 44, 45]. Another fascinating area of use is ultra-sensitive force (zeptonewton range, 10^{-18} N) and torque (10^{-25} Nm range) measurement [46, 47].

The primary goal of my work was to design and develop an experimental apparatus for optical trapping in vacuum based on counter-propagating beams geometry. The essential parts of the developed experimental set-up are described in Chapter 2.

The ability to design and dynamically change the optical forces or to control the stochastic forces opened experimental ways to test fluctuation theorems [48], test information thermodynamics [49] or realize compression stages of heat engines [50]. I utilised the set-up to carry out an experiment studying the mechanical effect of polarisation dependent optical force on a trapped particle. The experiment, which was theoretically proposed by my colleague Stephen Simpson, is presented in Chapter 3. It shows, compared to the linearly polarised case, that the circularly

polarised light generates additional component of the total force on the particle which points in direction perpendicular to the light propagation and is proportional to the trapping power. Although this component is small, it drives the particle out of thermal equilibrium and it can even lead to ejection of the particle from the trap. We believe such optical traps using circularly polarized light are promising testbed for non/equilibrium statistical mechanics.

The ability of our set-up to levitate several particles simultaneously was also exploited. Those particles are coupled via optical forces which is known as *optical binding* [51]. This phenomenon is well examined in overdamped systems using water as ambient medium. On the other hand, the optical binding in vacuum is virtually unexplored and of growing interest due to possible link to quantum entanglement of 'macroscopic' objects [52]. Chapter 4 summarizes experimental observation of dynamics of several optically bound particles trapped in vacuum. Extra attention is paid to the simple case of two bound particles for which we identify normal modes, show the tunability of the interparticle separation and quantify the nonlinear interparticle coupling for various separations.

In Chapter 5 an universal method is introduced, which estimates the optical trap force field exerted on the particle only by evaluating the particles stochastic trajectory. It utilizes a binning approach to calculate local mean velocity and acceleration and it is applicable for arbitrary force field, conservative or non-conservative. The performance of the method is demonstrated on experimental data.

I contribution to the presented results mainly by experimental activity. I designed and aligned the experimental setup used in Chapter 3 and part of Chapter 4, including control software development. I performed majority of the experiments and part of the data processing. I was closely involved in discussions on the obtained results. I developed the estimation method presented in Chapter 5 practically on my own.

2 Experimental set-up

Compared to frequently used optical traps in water, stable and reliable trapping in low pressure is much more technologically demanding. In water the motion of the optically trapped bead is damped intensively by the surrounding medium. The trapped bead's motion is overdamped, the bead's inertia doesn't play a role and the trap is unlikely to be destabilized by mechanical instability or intensity noise of the trapping beam. The processes of interest are slow enough to be observed by common cameras and of-the-shelf quadrant detectors. The objects to be trapped float freely in the medium and can be trapped by moving the sample stage in the right direction. When the trapped object leaves the trap it is floating nearby the trapping location and can be easily trapped again. None of this is true for trapping in air and low pressure. For vacuum traps few of the traditional techniques can be used and novel techniques of trap design, alignment, sample loading and detection have to be developed. Since the development of the experimental set-up was the main goal of my PhD activity, it is presented in detail in the following paragraphs.

2.1 Optical forces

The forces exerted on a particle originate from momentum change of the photons scattered on it. The force acting on a particle located inside a single laser beam is traditionally decomposed into two components - the *gradient force* and the *scattering force*. This custom originates in the Rayleigh approximation of scattering [53, 54], which is used for description of optical forces acting on a particle, which is much smaller than the wavelength of trapping light and which can be described as an induced dipole. The scattering force, commonly known as radiation pressure force, acts in the direction of propagation of light and it pushes the particle out of trap. The gradient force is directed towards the region of highest intensity, provided the particle's refractive index ($n_{particle}$) is higher than that of surrounding medium (n_{medium}), and it pulls the particle back to the trap.

Geometric optics can be employed to get an intuition for the origin of the gradient force. Light is treated as a collection of rays which are refracted and reflected on the interface of the particle and the surrounding medium (see Fig. 2.1a). The photons following light ray A are refracted downwards, their direction of propagation is changed, meaning their momentum is changed also. According to Newton's second law of motion, this change in momentum is caused by a force acting on the photons and this force is generated by the material of the particle. According to the Newton's third law, if the particle exerts a force on the photons, the photons exert force on the particle and this force has the same magnitude and opposite direction. So the

refracted photons generate force $\mathbf{F_A}$ pushing the particle upwards. Similarly light ray B is refracted upwards and generates force $\mathbf{F_B}$ downwards. Since the intensity of A exceeds the intensity of B, the net force acting on the particle points upwards and the particle is drawn to the region of higher intensity - to the beam axis.

The particle, however, is also propelled forward, partly due to the reflection of light on the particle. In order to compensate for this destabilising force component and achieve stable confinement, A. Ashkin used two mildly focused counter-propagating beams in his first experiments [1]. Later he introduced the *levitation trap*, where the scattering force was counter-acted by gravitational force [55]. The most popular 3D trap uses one tightly focused beam forming so called *optical tweezers* [56]. Such single beam trap is depicted in Fig. 2.1b). The particle is displaced along the optical axes to the right from the focus. Rays C and D are refracted such that they propagate to the right in a more horizontal direction, generating restoring forces $\mathbf{F_C}$ and $\mathbf{F_D}$ on the particle pointing to the left towards the focus.

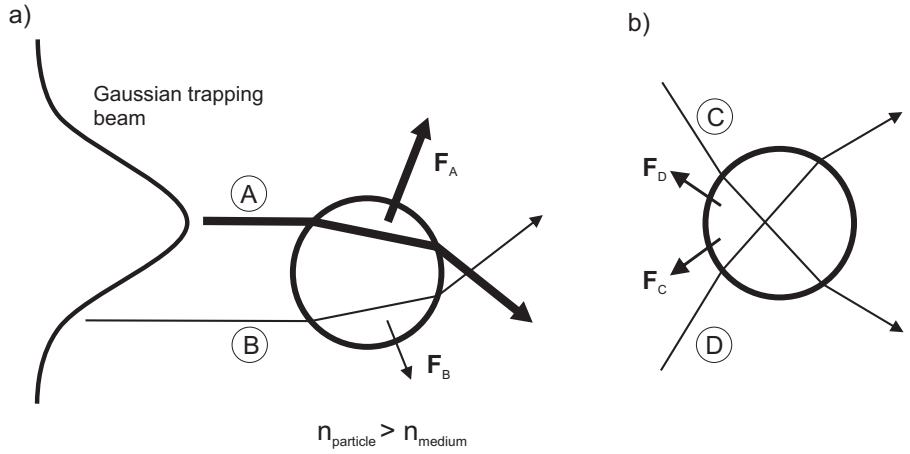

Fig. 2.1: Origin of optical forces using a geometric optics description (see details in the text).

2.2 Optical set-up

We decided to employ the counter-propagating geometry because of its universality, which gives the opportunity to perform wide range of experiments. In this geometry of beams the axial scattering forces from both beams cancel and only gradient force remains [57]. This configuration, also known as *dual beam* (DB) optical trap, uses two laser beams, which are coaxial, but propagate in opposite directions. To form a trap, the beams are mildly focused (typically NA > 0.5) and their fori are overlapped (see Fig. 2.2a,b)). Among the main advantages of DB belong the possibility to trap several objects or observation of trapped object perpendicularly to the beam axes.

Ashkin's original design of DB trap [1] did not employ interference of the counter-propagating beams and thus only one trap was generated (Fig. 2.2a)). When coherent and interfering light is used, standing wave is created (Fig. 2.2b)), which generates an axial array of many optical traps [12]. With respect to their sub-wavelength dimension, these traps are ideal for trapping of nanoparticles [58, 59, 60] and their transport by so-called *optical conveyor belt* [14, 61, 62]. Fig. 2.2c) shows an image of a microparticle trapped in DB vacuum optical trap I built in labs of the Institute of Scientific Instruments of the CAS in Brno.

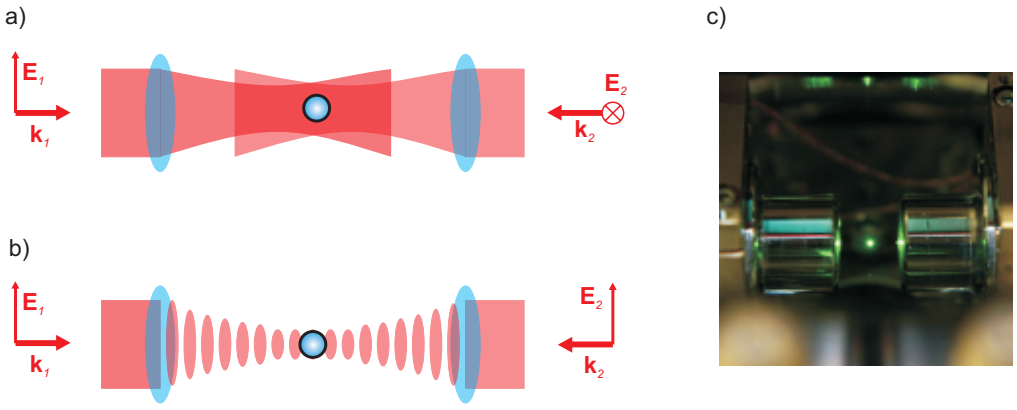

Fig. 2.2: Dual beam optical trap; (a) two counter-propagating beams with perpendicular linear polarisations do not interfere and one trap is created; (b) two counter-propagating beams with parallel polarisations interfere creating standing wave and array of traps; (c) a microparticle trapped DB optical trap in vacuum.

A schematic of our experimental set-up is provided in Figure (2.3). The low noise laser beam from a Prometheus laser (Coherent) emitting at wavelength of 1064 nm passes, first, through a polarizing beamsplitter PBS1 (Thorlabs PBS203) and then is coupled to a single mode optical fiber (SMOF, SQS 980 HP) for spatial filtering. The trapping power is controlled by rotation of the half-wave plate, PP1 (Thorlabs WPQ05M-1064), in front of PBS1. The output of the SMOF is divided into two beams of equal power and orthogonal linear polarization (LP) by polarizing beamsplitter PBS2 (Thorlabs PBS203). Lenses L3 (AC254-200-A) and L4 (AC254-200-C) constitute a 1/1 beam expander with focus located on dielectric mirror M1 (Thorlabs NB1-K13). For dual beam traps precise overlap of the foci of the counter-propagating beams is critical. Inspection and correction of the overlap inside vacuum chamber is generally complicated and time-consuming procedure. Involving beam expander enables us to assure good foci overlap and compensate mechanical drifts very efficiently. If the expander is adjusted correctly the focal plane of the trap inside the chamber is conjugated with the mirror M1 plane. This means that good overlap of beams in the M1 plain implies good overlap in the trap plain. Because

the mirror surface is not absolutely perfect, it scatters a little portion of the light so the overlap of beams foci in M1 plane can be observed by camera C1 and eventually corrected by tilting the mirror DM1.

Before entering the vacuum chamber, the polarization of one of the beams can be changed from linear to right-hand or left-hand circular (CP) by a quarter-wave plate PP4 (Thorlabs WPQ10M-1064). The linear polarization of the second beam can be first rotated through an arbitrary angle by half-wave plate, PP2 (WPH10M-1064), and subsequently changed from linear to right-hand or left-hand circular polarization by the quarter-wave plate, PP3 (Thorlabs WPQ10M-1064). In the vacuum chamber, the counter-propagating beams are focused by aspheric lenses L1, L2 (Thorlabs C240TME-C) of focal length 8 mm to create a trap with a beam waist of $w_0 \approx 2.7$ μm.

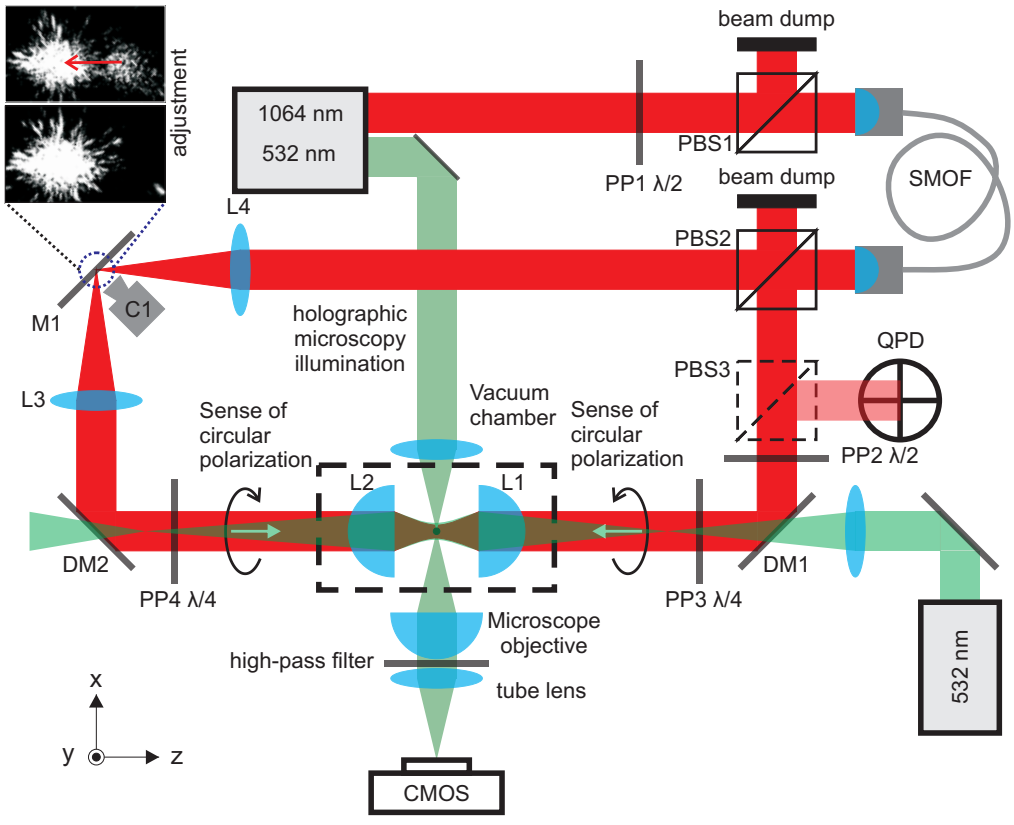

Fig. 2.3: Experimental arrangement.

2.3 Particle tracking

2.3.1 Split detection by quadrant photo-diode

We employed a detection scheme based on the back focal plane interferometry [63, 64, 65, 66]. A particle positioned in the trapping beam scatters a little portion of the trapping light. Both the scattered light and the unscattered trapping beam propagate towards quadrant photo-diode (QPD) plane, where they interfere. If the particle is not positioned in the centre of the trap, the interference intensity pattern is not centrally symmetric, as indicated in Fig. 2.4. The asymmetry of the intensity distribution encodes the particles position in the two lateral directions x and y, the total intensity encodes the axial position z. The positions voltage signals are generated from four separate quadrant signals Q_1 - Q_4 according to the following equations:

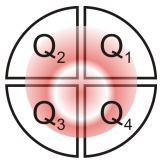

$$x = \frac{(Q_2 + Q_3) - (Q_1 + Q_4)}{Q_1 + Q_2 + Q_3 + Q_4}$$
$$y = \frac{(Q_1 + Q_2) - (Q_3 + Q_4)}{Q_1 + Q_2 + Q_3 + Q_4}$$
$$z = Q_1 + Q_2 + Q_3 + Q_4$$

Fig. 2.4: QPD detection principle.

In our case, one of the trapping beams (red coloured beam in Fig. 2.3) is used for the tracking the particle position. After passing through the vacuum chamber the measuring beam is reflected by the polarizing beamsplitter PBS3 onto the QPD. Half-wave plate PP3 is used to control the intensity reflected onto the QPD to set optimal signal-to-noise ratio.

Since the typical oscillation frequencies of trapped nanoparticles range from 10 kHz to 150 kHz and for example the rotational frequencies of trapped nanowires are even several orders of magnitude higher, commercially available quadrant detectors with the detection bandwidth (BW) of about 100 kHz are not fast enough. The bandwidth of these devices is limited mainly by the electronics, not the photodiode itself. Quadrant photodiodes with bandwiths up to 120 MHz are available so with appropriate amplifying electronics the detection BW can be significantly enhanced. In collaboration with electrical engineers we developed a QPD detection unit based on InGaAs quadrant photodiode Hamamatsu G6849. The four current signals generated by the quadrants are amplified and analogically processed into x, y, z voltage signals by summation electronics according to scheme depicted in Fig. 2.4. This detector provides us with detection BW of approximately 1.5 MHz. The position

voltage signals are acquired by NI USB 6351 acquisition card at 400 kHz sampling rate. The 1.5 MHz BW is given by the summation electronics. With modern acquisition and signal processing devices it is possible to sample the four quadrant separately and calculate the coordinates in a digital manner with sampling rates up to several hundreds of MHz.

2.3.2 Videomicroscopy

The particle's motion is also tracked from outside the vacuum chamber by videomicroscopy using a fast CMOS camera (Vision Research Phantom V611) which can be triggered to start recording at the same time as the QPD. The position is not known in real time, it is obtain by postprocessing of the recorded video using in house developed MATLAB code. Employing videomicroscopy brings some significant advantages over the QPD approach. First, more than one particle can be tracked. If more particles are trapped, for example during optical binding experiments, the QPD signal is a mixture of two motions which cannot be separated. Second, the microscope can be easily calibrated by calibration grid so the dimensions in the image are well known. In contrast, the QPD signal is a voltage signal and the relation between voltage and displacement expressed in meters has to be established by sophisticated methods using parameters of the trapped particle, which are not always well known [67, 68].

We set up a microscope composed of a microscope objective (MOTIC, Plan Apo, $100\times/0.55$, WD 13), tube lens (Thorlabs ACA-254-500A) and a fast CMOS camera (Vision Research Phantom V611) capable of recording up to 700 000 frames per second. Long working distance of our objective (13 mm) enabled us to observe the particle motion from outside the vacuum chamber. Still it was necessary to manufacture a vacuum viewport allowing us to put the objective barrel close enough to the trap. We manufactured such viewport by welding a stainless steel tube onto a blank flange with a hole in it. On the other end of the tube there is a microscope slide glued on. The flange mounted on the vacuum chamber creates a tunnel leading to the trap in which the objective is inserted.

The most straight-forward way how to observe a trapped particle by such microscope is to record the scattered trapping light without any additional illumination. The position of the bright spot in the image (viz. Fig. 2.5a) can be evaluated with sub-pixel precision when the intensity distribution is fitted by 2D Gaussian function or its centre of mass (centroid) is calculated. Particle position can be found, naturally, only for the two observed dimensions. Unfortunately the achievable frame-rate of such recording is limited by both the amount of light scattered and sensitivity of camera on used trapping wavelength. The camera we use is designed for recording

scenes illuminated by white light and it is the most sensitive in the green spectral region, the sensitivity on near IR is nearly zero. Since we trap with 1064 nm laser, this way our frame-rate would be very limited. Thus we employed wide horizontal green laser beam (532 nm) with low intensity to not affect the motion of observed particles and we observed the green scattered light as depicted in Fig. 2.3.

We also employ the so called holographic microscopy technique, which in principle provides us with all three coordinates of the particle position and moreover with its radius and refractive index [69, 70, 71, 72]. The particle is illuminated by wide Gaussian beam and it scatters a little portion of the incident light. The scattered light propagates to the microscope objective focal plane where it interferes with the unscattered beam. The interference pattern is then imaged by the microscope onto the camera CMOS chip (viz. Fig. 2.5b). The obtained intensity distribution is then fitted with physical model of scattering with fitted parameters being the 3D position of the particle, its radius and refractive index.

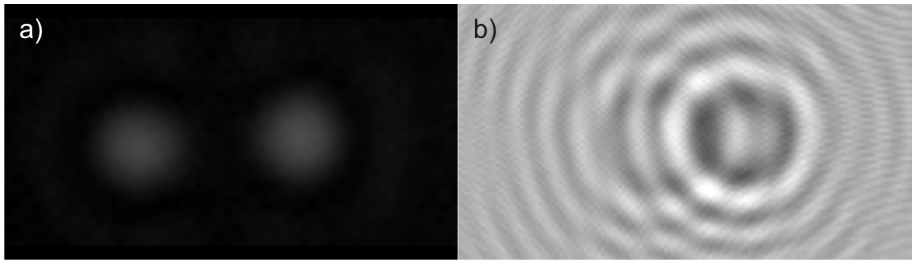

Fig. 2.5: Videomicroscopic observation of particles; (a) image of two trapped micro-particles using only scattered trapping light; (b) holographic image of two trapped micro-particles.

2.4 Particle loading

Loading a particle into a vacuum optical trap presents a surprisingly non-trivial problem. In liquid the procedure is straight-forward. A tenuous suspension of beads in water is prepared and it is injected into the experimental chamber (glass capillary, sample on microscope slide). The particle moves around the trap in a Brownian manner. By moving the sample stage accordingly, a desired particle can be moved to close vicinity of the trap and trapped. When the particle is lost, it stays nearby and can be trapped once more. On the other hand, particles in air cannot be manipulated in controlled manner to load the trap and when lost they fall down due to gravitational force and cannot be recaptured again.

2.4.1 Nebulisation

We implemented two methods of loading the vacuum trap, both relying on the bead reaching the trapping volume by chance. The technologically less demanding method uses an ultrasonic nebuliser. An ultrasonic nebuliser is a medical device which creates a spray of little droplets of a medicament which is then inhaled by a patient. It essentially consists of thin polymer mesh mount on the top of a piezoelectric ring. Suspension of beads in isopropyl alcohol (IPA) is put on one side of the mesh. When the nebuliser is turned on, the piezoelectric ring starts to oscillate thus pushing the suspension through the mesh and creating little droplets on the other side. The typical diameter of a droplet is $< 10\,\mu$m and the concentration of the suspension is such, that there is one or zero particle on average. Under standard atmospheric conditions the IPA evaporates quickly and a individual bead in air remains.

We use the commercial nebuliser Beurer IH50 which generates quite fast stream of droplets with inconveniently big spatial spread. Particles sprayed this way are too fast to be trapped and generally too far from the trap. In order to slow the droplets down and focus them near the trapping region we first generate a mist of droplets in a glass nozzle ended with a small opening (see Fig. 2.6a)). Then the droplets are pushed out slowly from the nozzle into the trap by air pumped into the nozzle by peristaltic pump. This way we get a dense stream of droplets falling slowly into the optical trap (Fig. 2.6c)) enabling us reliable loading of either single particle or chain of particles for optical binding experiments. The disadvantage of this method is the necessity of loading under air pressure and pumping down to target pressure afterwards. During initial phase of pumping the particles tend to be kicked out of the trap by airflow in the chamber which needs to be prevented by reducing the pumping speed substantially thus making this method quite time consuming.

2.4.2 Laser induced acoustic desorption

The second method of loading the particles into optical trap we implemented is laser induced acoustic desorption [73], also known as optical catapult. We spin-coat two or three layers of the beads on top of a silicon wafer ($200\,\mu$m thick). The particles are attracted to the surface by Van-der-Waals forces which need to be overcome in order to release the particles. Acoustic desorption aims at moving the surface sufficiently fast to shake the particles off. The necessary acceleration can be achieved by absorption of high power laser pulses. We put the wafer into the vacuum chamber approximately 5 mm under the optical trap reduce the pressure to 5 - 10 mbar. We hit the bottom side of the wafer by a single focused laser pulse of central wavelength 532 nm, spot diameter 300 μm and 10 - 15 mJ energy in pulse. The pulse is absorbed in the wafer and creates an acoustic wave propagating through it

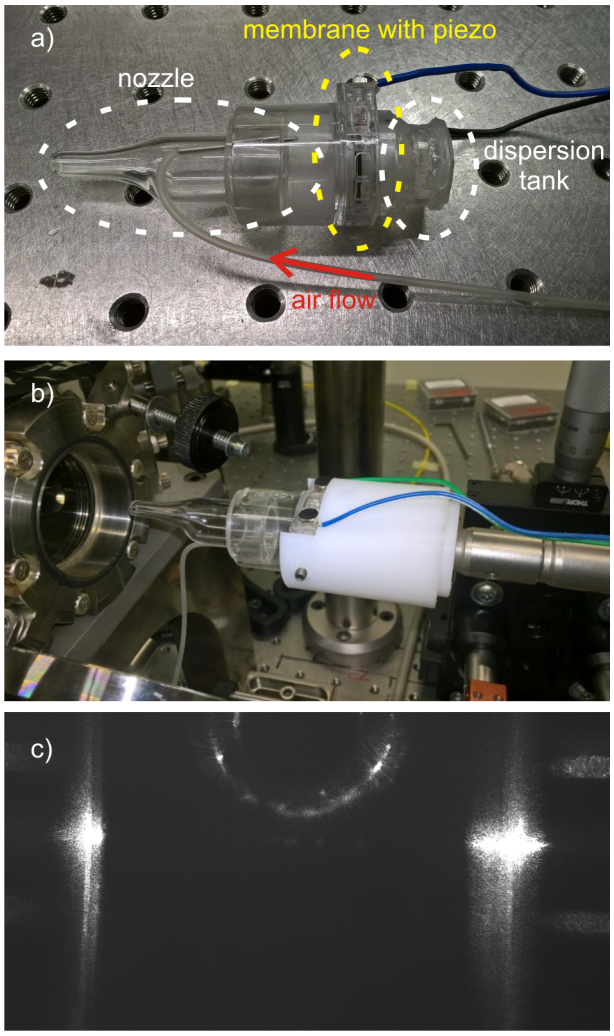

Fig. 2.6: Ultrasonic nebuliser modified for particle loading. (a) only the membrane with piezoelement is taken from the commercial nebuliser, a tank for the dispersion is glued on the back-side of the membrane, on the front-side a glass nozzle is attached with silicon ring. Air is pushed into the nozzle through a silicon hose. (b) The whole nebuliser is inserted into the chamber by sliding mechanism. (c) Droplets falling through the trapping beam.

to the top side [74], subsequently catapulting a cloud of beads upwards [75] to the optical trap (Fig. 2.7b)) from surface area of size comparable to the laser spot. The initial velocity of the catapulted beads and the height they reach depend on gas pressure and power density of the pulse hitting the wafer [73]. Basically the lower the pressure and the bigger the power density of the pulse, the higher the beads are catapulted. So fine-tuning these two parameters the beads can be catapulted in a way that by the time they reach the trap height they are slow enough to be trapped.

Apparently, after couple of pulses the beads from the surface area and the pulse

incidence spot has to be moved. Simultaneously the laser beam spot has to be placed under the trap quite precisely so the particles hit the trap. Little shift of the focus position can be done by tilting the beam in front of the focusing lens by mirror (Fig. 2.7a)) but after some more shots the whole wafer needs to be moved inside the vacuum chamber. We avoided the need for venting and opening the chamber by installing a simple wafer holder which can be moved from outside of the chamber. The holder consists of two teflon parts (Fig. 2.7a)). One part is placed inside the chamber, it is sitting on the bottom vacuum viewport under the optical trap and it is carrying the silicon wafer. This first part has pieces of steel installed in it. The second part of the holder is placed outside the chamber on the viewport and it incorporates set of neodymium magnets. The two parts are magnetically coupled and by shifting the outside part, the inside part is also shifted enabling us to adjust the wafer without the necessity of venting.

Compared to the nebuliser technique, the catapulting avoids the slow and problematic pumping from air pressure and if needed, a single particle can be loaded quickly again. From our experience, more than one particle are trapped extremely rarely and trying to trap additional particle by catapulting once more leads nearly always to losing the original one. So catapulting is not suitable for loading more than one particle. Additionally the optical access used for the pulsed laser optical path and the wafer holder cannot be used for anything else thus considerably restricting the experiment.

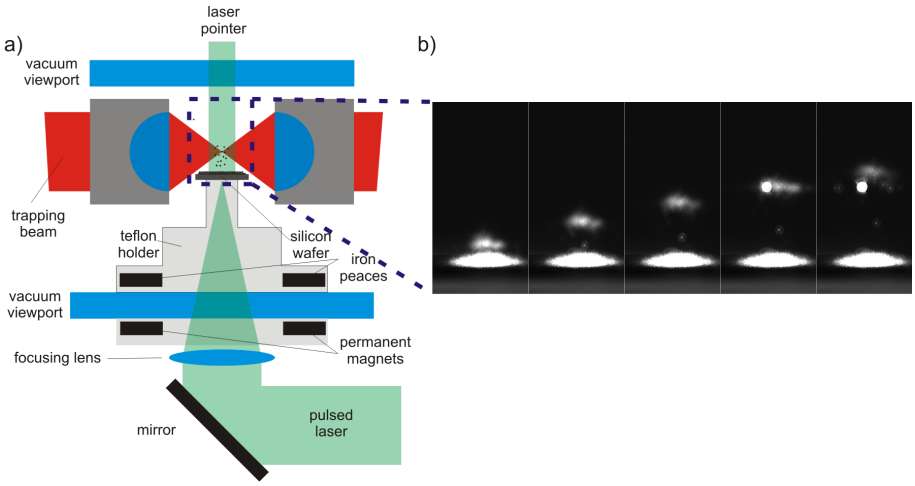

Fig. 2.7: Optical catapult. (a) geometry of the loading mechanism by optical catapult with movable holder; (b) cloud of catapulted particles ascending towards the trap and reaching the trap (bright spot on the right).

3 Transverse spin forces and non-equilibrium particle dynamics in a circularly polarized vacuum optical trap

The optically levitated particle became popular platform to study stochastic thermodynamics. The ability to design and dynamically change the optical potential or to control the stochastic forces opened experimental ways to test fluctuation theorems [48], test information thermodynamics [49] or realize compression stages of heat engines [50]. In the presented paper we show that an optical trap consisting of two counter-propagating circularly polarized laser beams gives rise to a non-conservative force field in azimuthal direction which drives the particle out of thermal equilibrium. Depending on the conditions, the dynamics of the particle can range from stochastic motion near thermal equilibrium to stable orbital motion around the optical axes, rendering such optical traps promising testbed for non-equilibrium statistical mechanics.

Second intriguing aspect of this experiment is the origin of the azimuthal component of the optical force itself. According to Newton's third law, the optical force acting on a particle emerges as a result of change of momentum of photons. Consequently, the momentum of light can be studied by observing mechanical effect of light on a probe particle. The observed dynamics is a manifestation of mechanical effect of optical spin. Spin angular momentum is given by the polarization state of the light beam, linearly polarised light having zero and circularly polarised light having maximal spin [76, 77]. Under certain circumstances the spin angular momentum generates a spin dependent component of linear momentum of the beam, $\mathbf{p}^S$, which tends to point in transverse direction [76, 78, 79]. This component of the linear momentum was previously thought to be virtual and unmeasurable. Here, its effect is revealed in the inertial motion of a probe particle in a circularly polarized Gaussian trap, in vacuum.

The results presented below in this chapter is a typical example of our team collaboration. I was responsible for design, development and operation of the experimental setup (described in detail in Chapter 2). I also carried out all the measurements and performed part of data processing.

3.1 Introduction

Although its existence has been recognized since the time of Kepler, the momentum of light remains a subject of intense debate. Uncertainty over its value when propagating through continuous media continues to excite interest [80]. Even in free space the topic is not without controversy. For example, the time averaged Poynting momentum in free space can be separated into two parts [77, 76, 79] whose differing properties have yet to be fully understood:

$$\mathbf{p} = \frac{1}{2c^2}\Re\left(\mathbf{E}^* \times \mathbf{H}\right) = \frac{\epsilon_0}{2\omega}\Im\left[\mathbf{E}^* \cdot (\nabla)\mathbf{E}\right] + \frac{\epsilon_0}{4\omega}\nabla \times \Im\left[\mathbf{E}^* \times \mathbf{E}\right] \equiv \mathbf{p^O} + \mathbf{p^S}, \quad (3.1)$$

(in SI units, with c the speed of light, and ϵ_0 the permittivity, in vacuum). The first of these contributions, $\mathbf{p^O}$, is independent of polarization, and referred to as the orbital component. The second term, $\mathbf{p^S}$, is related to inhomogeneous circular polarization, and referred to as the spin component. Eq. (3.1) is the most appropriate since the different components, $\mathbf{p^S}$ and $\mathbf{p^O}$ couple to dielectric matter in qualitatively different ways for dielectric objects of small or intermediate size [81, 78, 82].

The question of how and, indeed, if $\mathbf{p^S}$ couples to matter presents itself. Addressing this issue is experimentally challenging. Spin momentum ($\mathbf{p^S}$) requires field inhomogeneities which, by necessity, generate other forms of optical force, including gradient forces. To measure its effect, delicate spin forces must be reliably distinguished from other, stronger forces. This was elegantly achieved in a recent experiment, in which the deflection of a nano-cantilever, immersed in a circularly polarized evanescent field was measured [81]. In this case the spin dependence of the force is isolated, from the prevailing effects of orbital momentum, by varying the degree of circular polarization, applying a symmetry argument and by observing that, in an evanescent wave, spin and orbital components of momentum are orthogonal [78, 78]. Other experiments require minute analysis of the motion of particles in liquid, subject to appropriate light fields [83, 84]. Related or analogous effects rely on substrate interactions or optical chirality or birefringence [85, 86, 87, 88] and, whilst fascinating in their own right, do not depend explicitly on incident spin momentum.

In this work, we consider the motion of a probe microsphere in an almost paraxial, circularly polarized Gaussian vacuum trap. For this purpose we use the experimental arrangement described in Chapter 2. Pronounced departures from equilibrium behaviour are observed which demonstrate the presence of transverse spin forces deriving from corresponding components of optical momentum.

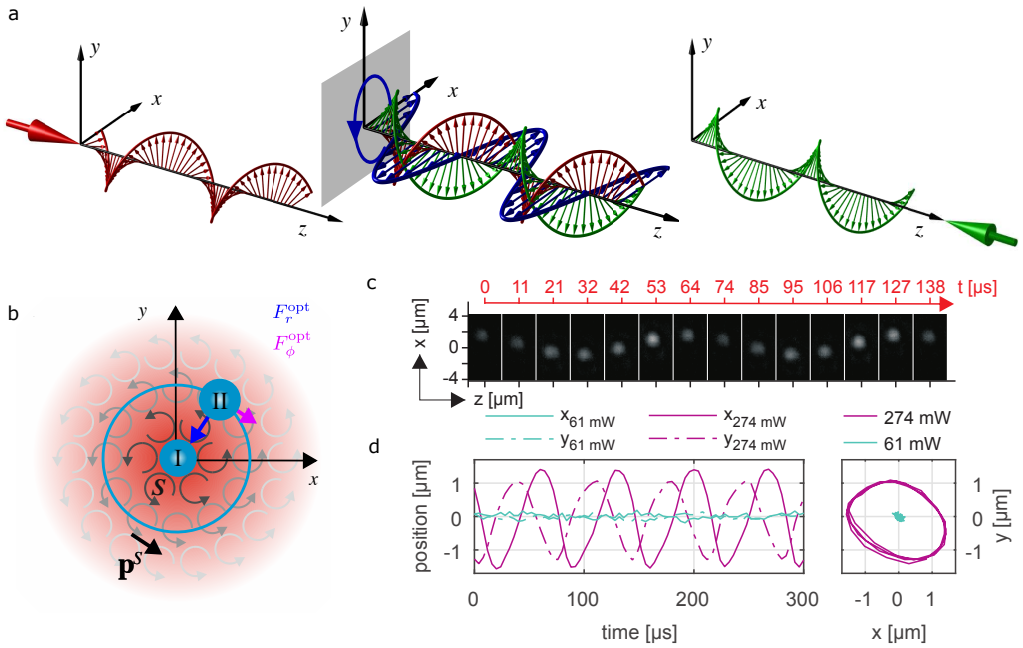

Fig. 3.1: Physical principle. (a) Schematic showing the electric fields in the counter-propagating circularly polarized beams of opposing handedness (green and red) and the rotation of the combined electric field (blue). (b) Local optical spin ($\mathbf{S} = \Im(\mathbf{E}^* \times \mathbf{E})$) field in the transverse xy plane of the beam. Radial gradient optical force F_r^{opt} and azimuthal non-conservative spin force, F_ϕ^{opt} acting upon a particle positioned off-axis. Regime I corresponds to the particle position in the vicinity of the beam axis for lower laser power while regime II corresponds to the above threshold condition, in which the particle orbits the beam axis. (c) Snap shots of orbiting particle (regime II) taken by the CCD camera oriented perpendicularly to the beam propagation. (d) Trajectories of the particle for both regimes I and II acquired by a QPD. Turquoise curves denote trajectories for a lower trapping power of 55mW with particle motion near the beam axis; pink trajectories show an orbiting particle for an above threshold power of 180mW.

3.2 Results

In our experiments, spin forces manifest themselves directly, through the inertial motion of a microsphere in a vacuum optical trap, in free space. By comparison with the relatively subtle effects previously observed, our results are striking and unequivocal. Ultimately, we observe the violent ejection of a probe particle from an optical trap, as a direct consequence of transverse optical spin momentum. The experiment itself is elegant in its simplicity. We track the motion of a small, dielectric probe particle in a counter-propagating Gaussian beam trap, in vacuum (see Fig. (3.1a,b)). The beams are weakly focused with a numerical aperture of NA ≈ 0.18

(equivalent to a Rayleigh range of $kz_{\mathrm{R}} \approx 150$, for wave-vector k). This symmetric geometry nullifies the axial scattering forces associated with each beam [89] and emphasises transverse spin components, when they are present. The polarization state of the beams can be independently adjusted using quarter wave plates on either side of the trap. When the beams have parallel, linear polarization (LP), the only surviving forces in the trap are optical gradient forces. Since gradient forces are conservative, thermal equilibrium is maintained within the trap, equipartition of energy holds, $\frac{1}{2}k_{\mathrm{B}}T = \frac{1}{2}K_i\langle x_i^2\rangle$, where K_i is the trap stiffness in direction i. So the greater the power in the trap is, the more tightly the particle is constrained i.e. $\langle x_i^2\rangle \propto 1/P$.

When the quarter-wave plates are adjusted so that the beams are circularly polarized with opposite handedness (CP) the electric field vectors of the beams rotate together, in the same sense, Fig. (3.1a). This has two effects. First, the weak focusing by the lens produces small, transverse components of $\mathbf{p^O}$ through spin-orbit coupling [90]. Second, the inhomogeneous circular polarization generates transverse components of $\mathbf{p^S}$, which also circulate about the beam axis, Fig. (3.1b). The spin term is strongly dominant, with $p_\phi^{\mathrm{S}}/p_\phi^{\mathrm{O}} \gtrsim (2kz_{\mathrm{R}}) \approx 300$ (see supplementary information of [91]). These transverse momenta give rise to azimuthal forces, primarily associated with $\mathbf{p^S}$. In combination with the optical gradient forces, the circularly polarized trap has a cylindrically symmetric force field, $\mathbf{F}^{\mathrm{opt}} = F_\phi^{\mathrm{opt}}\mathbf{e}_\phi + F_r^{\mathrm{opt}}\mathbf{e}_r$. For small displacements from the axis the gradient force, F_r^{opt}, is restoring, attracting the particle towards the center of the beam. The azimuthal component, F_ϕ, makes the trap non-conservative (i.e. $\nabla \times \mathbf{F}^{\mathrm{opt}} \neq 0$), forcing it out of equilibrium and allowing the particle to accumulate angular momentum.

The motion of the probe particle is determined by the delicate interplay between thermal fluctuations, spin and gradient optical forces and is governed by a Langevin equation, in Cartesian coordinates:

$$\mathbf{F}^{\mathrm{opt}}(\mathbf{r}) + \mathbf{F}^{\mathrm{L}}(t) - \xi\dot{\mathbf{r}} = m\ddot{\mathbf{r}}, \tag{3.2}$$

where m is the mass of the particle and ξ the pressure dependent Stokes' drag. $\mathbf{F}^{\mathrm{opt}} \equiv P\mathbf{f}^{\mathrm{opt}}$ is the external optical force at power P and $\mathbf{F}^{\mathrm{opt}}$ is the fluctuating Langevin force which is uncorrelated in time with zero mean and variance given by the fluctuation-dissipation theorem e.g. $\langle F_i^{\mathrm{L}}(t)\rangle = 0$, $\langle F_i^{\mathrm{L}}(t) \otimes F_j^{\mathrm{L}}(t')\rangle = 2k_{\mathrm{B}}T\xi\delta_{ij}\delta(t-t')$ for Cartesian components $i, j = x, y, z$. For CP beams we observe two distinct regimes (see depiction in Fig. (3.1c,d)), dependent on optical power. These can be contrasted with the conspicuously different behaviour observed in LP traps, which is qualitatively similar for all trap powers. At low optical powers (**regime I**) the particle undergoes non-equilibrium Brownian motion, deviating substantially from the equipartition of energy. At higher powers (**regime II**) we

observe the formation of stable orbits, which are thermally excited and driven by optical spin.

3.2.1 Regime I: Driven Brownian Motion

In the **low power regime I** (turquoise curves, Fig. (3.1d)), the particle remains within the linear range of the trap and, in Cartesian coordinates, the optical force can be approximated as,

$$\begin{bmatrix} F_x^{\text{opt}} \\ F_y^{\text{opt}} \end{bmatrix} = - \begin{bmatrix} K_r & K_\phi \\ -K_\phi & K_r \end{bmatrix} \begin{bmatrix} x \\ y \end{bmatrix}. \tag{3.3}$$

K_r is the radial stiffness associated with the gradient force. It is isotropic and gives a force in the radial direction, towards the origin. K_ϕ is the stiffness of the azimuthal force. Both stiffness coefficients are proportional to power e.g. $K_r = Pk_r$ and $K_\phi = Pk_\phi$. A threshold power $P = P_0$ constitutes a boundary between regime I and II, which is achieved when average centripetal forces acquired by the Brownian particle are just sufficient to balance attractive, gradient forces.

In regime I, where the power is below threshold ($P < P_0$), the stochastic motion of the probe particle can be characterised in terms of the power spectral density (PSD) and the time correlations of the particle coordinates both of which depend qualitatively on the presence of spin forces (i.e. on whether or not $k_\phi = 0$).

In both cases, the power spectral density of the system is dominated by a single peak, approximately at the resonant frequency, $\omega_0 = \sqrt{Pk_r/m}$. For conservative, linearly polarized beams, the peak height decreases with increasing optical power ($\propto 1/P$) and has a constant width associated with the drag term.

For very low optical power, the circularly polarized trap behaves similarly. However, as the power increases and approaches the threshold, P_0, a qualitative difference emerges and the peak grows in height, $\propto 1/(P_0 - P)^2$, while decreasing in width in proportion to $\Im(\omega_c) \approx \frac{\xi}{2m}\frac{(P_0-P)}{2P_0}$. Physically, the white thermal noise excites a resonance in which frictional losses are increasingly compensated by the non-conservative spin forces and the behaviour becomes increasingly coherent and deterministic. In this respect the behaviour of the trap is analogous to that of a laser approaching the lasing threshold. These theoretical predictions are supported by the experimental results in Figs. (3.2).

Time correlations $\langle x(t+\tau)x(t)\rangle$ and $\langle y(t+\tau)x(t)\rangle$ are in general damped oscillations. As $P \to P_0$, the amplitude of $\langle x(t+\tau)x(t)\rangle$ increases as $1/(P_0 - P)$, and decays increasingly slowly with time. Meanwhile, $\langle x(t+\tau)y(t)\rangle$ has the same amplitude, but is phase shifted by $\pi/2$, indicating a growing tendency towards rotation of

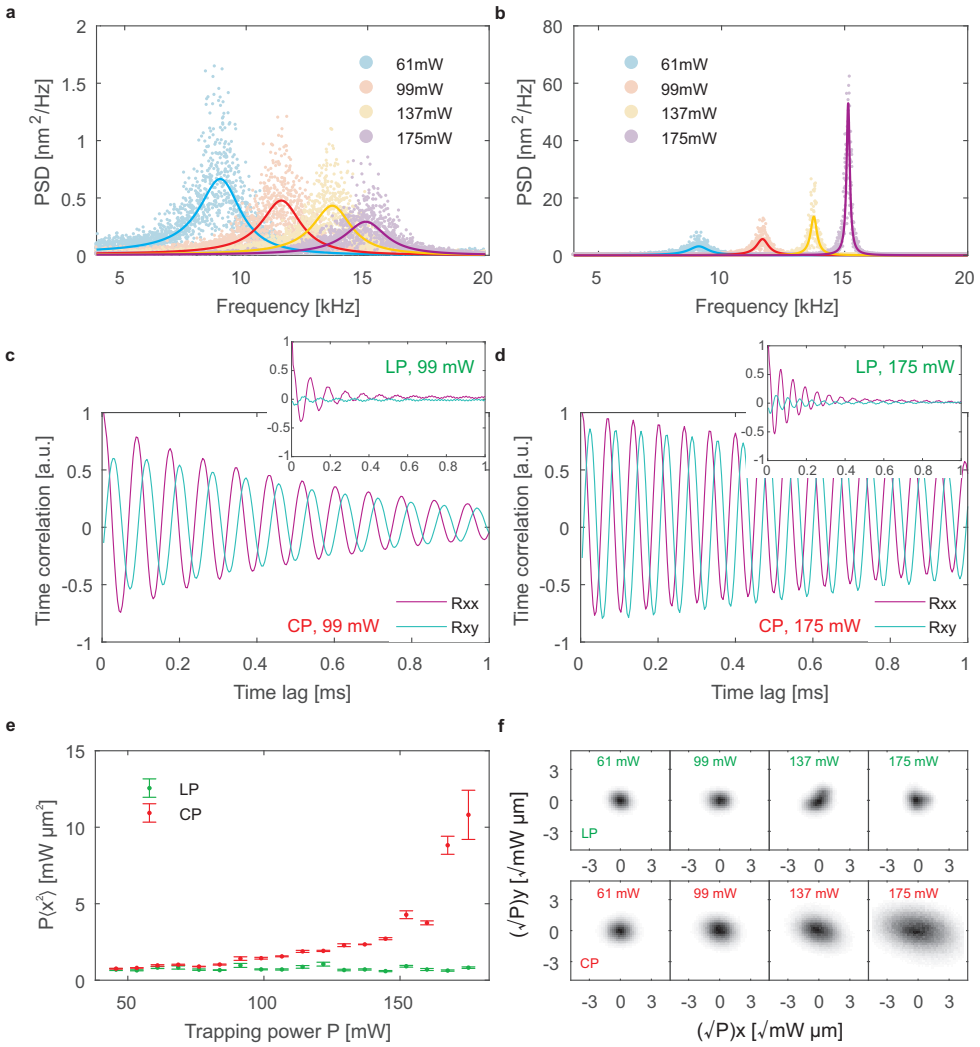

Fig. 3.2: Power spectral densities for particle positions for (a) LP (b) CP beams. In the latter case, spin momentum drives a resonance, increasing the peak height and narrowing its width. (c) and (d) time dependent variance of particle coordinates at two different beam powers. $\langle x(t+\tau)x(t)\rangle$ and $\langle x(t+\tau)y(t)\rangle$ are $\pi/2$ phase shifted, indicating a tendency towards circular motion. Increasing the power increases the mean frequency of rotation and increases the time constant governing the loss of coherence of the oscillation. Results for linearly polarized beams are inset. (e) Graph showing the product of the position variance with power, as a function of power ($P\langle x^2\rangle$ v P), for LP and CP. Error bars show the standard error of the mean. (f) Measured probability distribution of the trapped particle in the transverse plane, scaled by the square root of the beam power for a linearly polarized trap (top row) and a circularly polarized trap (lower row). Variation of this distribution with beam power indicates deviation from thermodynamic equilibrium.

the center of mass about the beam axis. Experimental results strongly support this idea, see Figs. (3.2c,d). Once more, they clearly demonstrate an increase of motional coherence for circularly polarized beams for powers approaching the threshold power.

For zero time ($\tau = 0$), the instantaneous variances of the particle coordinates, e.g. $\langle x^2 \rangle$, quantify the departure from thermodynamic equilibrium. In a conservative, harmonic trap (i.e. linearly polarized beams) equipartition is satisfied and the elastic and thermal energies can be equated e.g. $\frac{1}{2}Pk\langle x^2 \rangle = \frac{1}{2}k_{\mathrm{B}}T$, so that the product, $P\langle x^2 \rangle$ is constant. In contrast, the circularly polarized trap deviates increasingly from equipartition as P_0 is approached, so that $\langle x^2 \rangle \propto 1/(P_0 - P)$ increases rapidly, as confirmed experimentally in Fig. (3.2e). Figure (3.2f) illustrates this phenomenon visually: the two-dimensional probability density distribution of the trapped particle in the transversal plane, scaled by the square root of the beam power, is invariant for a conservative trap but grows with increasing power in the presence of non-conservative forces.

In combination, the PSD, time correlations and variances reveal the underlying physical behaviour. Optical forces vanish on the beam axis and are locally restoring so that points on the beam axis are mechanical equilibria. Nevertheless, thermal fluctuations repeatedly push the particle off axis, exposing it to the small, azimuthal spin forces. These increase the tendency for the particle to orbit about the beam axis, as expressed by the time correlations, $\langle x(t+\tau)y(t) \rangle$ and $\langle x(t+\tau)x(t) \rangle$. Centripetal forces grow and act against the gradient forces, effectively cancelling them as $P \to P_0$. Under these conditions, the stochastic motion becomes increasingly coherent in terms of rotation: kinetic energy is increasingly concentrated at a single, resonant frequency as indicated in the PSD (Fig. (3.2b)).

As the power is increased above P_0, centripetal forces tend to exceed gradient forces, and the particle is pushed outward. If the force field were truly linear, this process would continue indefinitely. In reality, the trap is finite. Stable orbits with well defined radii, r_{o}, and frequency, Ω, can form as the particle encounters non-linear regions of the trap, taking us into the **high power regime II** (purple curves, Fig. (3.1d)).

3.2.2 Regime II: Stable Orbits

Simple equilibrium conditions for the orbits can be obtained by balancing azimuthal spin forces with viscous drag, and radial centripetal forces with optical gradient forces:

$$\frac{P_\mathrm{o}}{\xi^2} = -\frac{r_\mathrm{o}}{m}\frac{f_r(r_\mathrm{o})}{f_\phi^2(r_\mathrm{o})}, \tag{3.4a}$$

$$\frac{\Omega_\mathrm{o}}{\xi} = \frac{f_r(r_\mathrm{o})}{m f_\phi(r_\mathrm{o})}, \tag{3.4b}$$

where P_o is the optical power required to sustain an orbit with radius r_o for a given viscous drag, ξ. Because the ratio of the azimuthal and radial forces is approximately constant the orbit frequency, Ω_o, is also approximately constant and independent of orbit radius and optical power i.e. $\Omega_\mathrm{o} \approx \Omega$.

This overall behaviour is confirmed experimentally. Figure (3.1c) illustrates the qualitative difference in the transverse motion of the particle between regimes I and II. This is quantified in Fig. (3.3a), which shows the mean values of the radius of the orbit as a function of optical power. Insets show that the orbit is slightly elliptical and its size suffers hysteresis with respect to the direction of power change. At the lowest powers the mean radii of the particle trajectories are indeed comparable for CP and LP beams. However, they begin to diverge with increasing power; the LP radii decrease and CP increase, in accordance with theory. At higher optical powers than those represented in the graph, centripetal forces exceed gradient forces and the particle is radially ejected from circularly polarized traps.

Mean values for x and y trap frequencies ($\omega_0/2\pi$) in LP traps are shown in Fig. (3.3b) and, together with the CP results, they follow the predicted behaviour. In regime I, CP and LP traps follow the same power dependence, however in regime II the orbiting frequency remains constant, the exact value depending slightly on the branch of the hysteresis curve. This reflects the observation that the ratio of the radial and azimuthal forces is approximately constant, yielding a constant orbit frequency in Eq. (3.4b).

Finally, Fig. (3.3c) shows the measured azimuthal force as a function of radius. This data is evaluated by fitting to experimentally measured trajectories as described in the Methods section of Ref. [91]. In particular, the curve was evaluated by fitting experimental PSDs to theoretical profiles for regime I, and by applying the orbiting equation, Eq. (3.4b), in regime II. The validity of the theoretical description is further demonstrated by the close overlap of the data points in the transitional region between axial motion and fully developed orbiting. For comparison, the continuous black line in Fig. (3.3c) shows the theoretical optical force, calculated from Mie theory. This agreement requires the theoretical optical power to be scaled by a factor of ≈ 2, which includes various uncertainties in the experimental system.

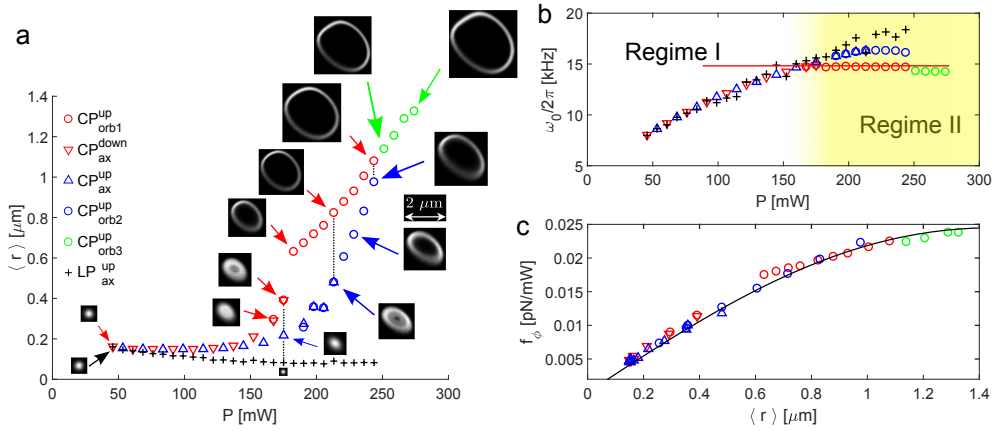

Fig. 3.3: Graphical comparison of the key physical quantities in regimes I and II. (a) Mean value of the orbit radius, $\langle r_o \rangle$, as a function of optical power. The insets show the probability density of the particle positions in the lateral xy plane relative to the given scale bar. Data related to circularly polarized beams (CP) are denoted by ◯, △ and ▽ for the orbiting regime II. △ and ▽ symbols correspond to increasing and decreasing optical power, respectively. For comparison data corresponding to parallel linear polarization (LP) are marked by black + signs. The sequence in which the data was acquired is indicated by colors and markers ◯, ▽, △, ◯, +, and ◯. Overlapping points ◯ with ▽ and △ with ◯ illustrate how different calculation methods, used for regime I and II, overlap in the region where the orbiting is not fully developed. (b) Resonant trap frequency $\omega_0/2\pi$ or orbiting frequency $\Omega_o/2\pi$ for regime I or II, respectively. The theoretical value from Eq. (3.4b), is indicated by the horizontal red line. Measured values of ξ/m, and calculated values of f_r/f_ϕ have been used. (c) Spin force, f_ϕ, for a particle of radius 770 nm and density 2200 kg m^{-3}. The presented values were determined as the mean value for x and y directions from fits to the PSD for regime I and from the orbiting equation (Eq. 3.4b) for regime II (see details in [91]). The black curve shows the theoretical force, obtained from generalized Lorentz Mie theory. A single scaling parameter has been used.

3.3 Discussion

Our experiments vividly demonstrate the mechanical effects of optical spin momentum. Spin forces bias Brownian motion, induce orbits and ultimately throw a probe particle from an optical trap. These results are completely generic: for a given particle and circularly polarized beam, at a given air pressure, there is always an escape power above which the trap will eject the particle. For fixed optical power, there is also an equivalent pressure beneath which the same thing will happen.

In addition, this work provides an archetypal example of linearly non-conservative optical vacuum traps. All of the phenomena observed here arise from intrinsic, non-symmetric coupling between motional degrees of freedom. This is expressed in the asymmetry of the stiffness matrix, Eq. (3.3). For circularly polarized light, this coupling is caused by spin. More generally, asymmetric coupling can be induced by any reduction in symmetry, either of the particle shape, or the trapping field [92]. In viscous media, this results in biased Brownian motion [93]. As we have seen, the consequences in air or weak vacuum are more extreme, since the trapped particle can accumulate momentum, resulting in thermally excited coherent motion. Analogous effects may be expected for non-spherical particles or defective beams.
Finally, these experiments signpost a new research direction. Optical force fields are generally non-conservative, and their structure is derived from internal momentum flows. It is clear that measuring the trajectories of probe particles in vacuum can help us develop our understanding of optical momentum flows in structured light fields as well as the dynamics and thermodynamics associated with motion in potentially complex force fields. Some of these possibilities have previously been described by Berry and Shukla [94, 95]. Nevertheless, major unanswered questions persist, especially concerning the details of momentum coupling to matter of varying shape and composition, and to the interplay between thermal fluctuations and some of the dynamical behaviour predicted elsewhere.

4 Optical binding of microparticles in vacuum

More complex system of oscillators can be created by simultaneous trapping of multiple dielectric particles. The trapping light scattered by one particle can modify the trapping light field in location of some other particle, thus modifying the optical forces felt by the second particle. This also works the other way around, the second particle scatters trapping light, thus modifying the optical forces felt by the first particle. If such situation occurs, the two levitated particles become two coupled oscillators in a similar manner two pendulums would be coupled by a spring between them. This phenomenon of coupling mediated by scattered light is usually called *optical binding*, we say that the two particles are optically bound.

While optical binding in water (overdamped regime) was studied extensively [96, 97, 9, 98, 99, 51], systems of optically bound particles in vacuum (underdamped regime) are quiet unexplored. Such systems are believed to be excellent platforms for experimental investigation of as intriguing collective effects as selforganization [100] or synchronization [101]. So far, dynamics of particles trapped in two parallel optical tweezers in vacuum has been investigated [102] and experimentally very challenging trapping of optically bound array trapped inside a hollow core optical fiber was shown [[103]].

In this chapter, we investigate optical binding between multiple silica particles with identical sub-micron diameters confined in vacuum using two non-interfering, counter-propagating Gaussian beams with mutually orthogonal linear polarizations. We concentrate on the collective dynamics of optically bound matter in the underdamped regime at low ambient pressures. We observe the appearance of normal modes of vibration in the thermally driven particle motion, reconstruct the optical binding forces from experimentally recorded particle trajectories, quantify the level of non-linear coupling between the particles, and investigate the influence of the beam intensity profiles on the particle dynamics. We compare our experimental findings with the predictions of a quantitative theoretical model of particle interaction via optical and hydrodynamic forces, and observe a very good agreement. In addition, in the full version of this thesis we discuss the regular collisions of the particles at pressures around 1 mbar we observed.

I performed the first preliminary experiments with two and three optically bound particles trapped in cross-polarized counter-propagating beams using the experimental setup described in Chapter 2. I observed the collective dynamics similar to that presented in Fig. 4.2 and did the measurement of collective dynamics of three particles (presented in the full version of this thesis). I also observed and captured

collision of particles (discussed in the full version of this thesis) and performed part of the data processing (particle position tracking form video and analysis of particle trajectories). I participated in development of the theoretical models (see full version of this thesis), which arose from cooperation between me, S. Simpson, O. Brzobohatý and M. Šiler.

The first setup mentioned above did not allow us to easily modify the beam parameters for tuning the inter-particle distance as shown in Fig. 4.3. Also it took unbearably long (typically hours) for two or more particles to reach the trap. So another setup was used for detailed parametric study (see Fig. 4.1). It employed spatial light modulator (SLM) for trapping beam shaping. It also employed miniature vacuum chamber fitted between trapping lenses which proved more experimentally convenient in terms of optical path adjustment and speed of loading more particles.

4.1 Experimental configuration.

In our optical binding experiments, we used the trapping geometry with two horizontal, counter-propagating laser beams with wave vectors **k**, laterally overlapping in a vacuum chamber so that the beam axes were aligned along the same line [104] (see Fig. 4.2a) and 4.1 for illustration). The focal planes of the two beams with vacuum wavelength $\lambda = 1064$ nm and identical beam waist radii w_0 that could be varied in the range between 1.3 and 2.8 μm were separated by a distance of $\leq 5\mu$m to enhance the axial stability of optically confined SiO_2 (silica) particles with nominal diameters $d = 600$ nm [98]. The polarization of the two input beams was controlled with a pair of half-wave plates to form a cross-polarized dual-beam trap [91, 104]. Using video microscopy, the positions of the optically trapped and bound particles could be tracked in the $x - z$ plane with the temporal resolution of $\sim 3.3\,\mu$s and the spatial resolution of $\sim 10\,$nm (see Methods for additional details). As the strength of transverse optical trapping in the $x - y$ plane is significantly higher than the axial trapping strength along the z-direction, the trapped particles tend to migrate to the common axis of the two beams and form a quasi-one-dimensional (1-D) structure oriented along the z axis [105, 98, 99]. Figure 4.2a) illustrates how the scattered photons modify the distribution of light intensity in the simplest case of two optically trapped particles. For each of the two counter-propagating incident beams, the light scattered in the beam propagation direction denoted by **k** locally increases its optical intensity, whereas the back-scattered wave interferes with the corresponding co-polarized incident beam, creating *a weak standing wave along the optical axis* [106].

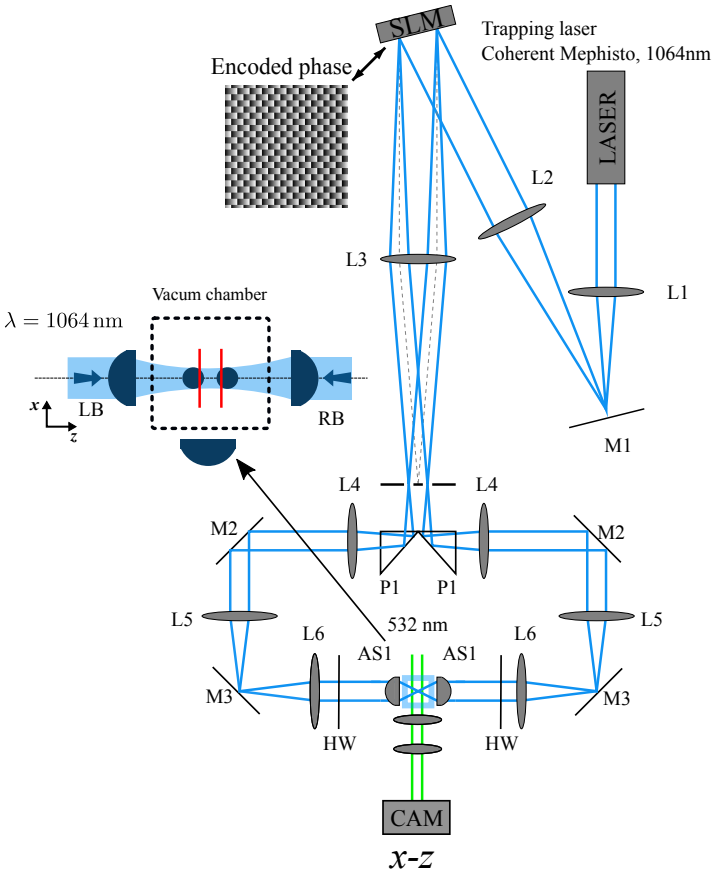

Fig. 4.1: Experimental set-up of the dual-beam optical trap. We used infrared laser light with vacuum wavelength of 1064 nm (Coherent Mephisto). A collimated Gaussian beam from the laser was projected on a spatial light modulator (SLM). Phase mask encoded at the SLM diffracted the beam into the ± 1 diffraction orders that generated the two counter-propagating trapping beams. Lenses L4 formed telescopes with the lens L3, projecting the SLM plane on the mirrors M2 and telescopes consisting of lenses L5 and L6 then imaged the SLM plane onto the back focal planes of aspheric lenses AS1 ($f = 8$ mm, maximal NA $= 0.5$) that focused the two trapping beams into the vacuum chamber. The focal planes of the two beams created in the trapping region were slightly displaced from each other (by approximately 5 μm, red lines) to increase the axial trapping stability [98]. The sample was illuminated by an independent laser beam (vacuum wavelength 532 nm) of waist radius of $w_0 = 40\,\mu$m propagating along the y-direction perpendicular to the imaging xz-plane. Low power (5 mW) of the beam ensured its negligible contribution to the net optical force. The motion of the particles in $x - z$ plane was recorded by a fast CMOS camera (Vision Research Phantom V611) with frame rate of 300 kHz. The off-line tracking of the particle position from the high-speed video recordings was based on the determination of symmetries in the particle images [107].

4.2 Linearly coupled harmonic oscillators.

A system of N optically and hydrodynamically interacting particles moving in an external optical trapping potential can be described as a set of N coupled damped harmonic oscillators. With an appropriate coordinate transformation, this set can be represented by an equivalent system of N uncoupled linear oscillators, whose resonant frequencies define the *normal modes* of the system. In particular, oscillatory dynamics of two elastically coupled particles can be fully characterized by two normal modes: the *centre-of-mass* (COM) mode, in which the two particles oscillate in phase within the external trapping potential while their separation distance remains constant, and the *breathing* (BR) mode, in which the particles oscillate out-of-phase, so that the centre of mass of the system does not move whereas the particle separation distance periodically changes [108]. Along the z-axis, the transformations from the absolute positions of the particles, $z_1^{\mathrm{a}}, z_2^{\mathrm{a}}$, to the normal-mode coordinates, $z_{\mathrm{COM}}, z_{\mathrm{BR}}$, with the corresponding resonant frequencies, $\omega_{\mathrm{COM}}^z, \omega_{\mathrm{BR}}^z$, read as (see Sections 1.4 and 1.6 in the Supplementary Information of [109]):

$$z_{\mathrm{COM}} = (z_1^{\mathrm{a}} + z_2^{\mathrm{a}})/\sqrt{2} \tag{4.1a}$$

$$(\omega_{\mathrm{COM}}^z)^2 = \frac{k}{m}\left\{1 - \frac{[1 - 3a/(2\langle\Delta z\rangle)]^2\xi_0^2}{4mk}\right\} \approx \frac{k}{m}, \tag{4.1b}$$

$$z_{\mathrm{BR}} = (z_2^{\mathrm{a}} - z_1^{\mathrm{a}} - \langle\Delta z\rangle)/\sqrt{2}, \tag{4.2a}$$

$$(\omega_{\mathrm{BR}}^z)^2 = \frac{(k+2b)}{m}\left\{1 - \frac{[1 + 3a/(2\langle\Delta z\rangle)]^2\xi_0^2}{4mk}\right\} \approx \frac{k+2b}{m}. \tag{4.2b}$$

Here, m is the particle mass, a is the particle radius, k is the stiffness of the external optical trapping potential created by the two counter-propagating beams, b is the effective stiffness of the binding interaction, $\langle\Delta z\rangle$ is the mean separation between the particles, and $\xi_0 = 6\pi\mu a$ is the particle's viscous drag coefficient, with μ being the viscosity of the surrounding fluid. Similar formulas hold along the x-axis, with $\langle\Delta x\rangle = 0$ in the expression for x_{BR} and k and b replaced with their transverse counterparts. As we operate in the underdamped regime with the damping ratio $\xi_0/\sqrt{4mk} \ll 1$, the normal-mode resonant frequencies, $\omega_{\mathrm{COM}}^{x,z}$, $\omega_{\mathrm{BR}}^{x,z}$, are approximately independent of the viscous friction [102]. Figures 4.2c) and 4.2d) show representative sequences of video frames recorded from two trapped, coupled particles in independent experimental runs. Depending on the actual initial conditions (particle position and velocity) at the time of entering the trap, the particles were observed to oscillate either in phase in the COM mode (see Fig. 4.2c) or out of phase in the BR mode (see Fig. 4.2d). In general, thermally driven motion of two coupled particles is a linear combination of the COM and BR normal modes

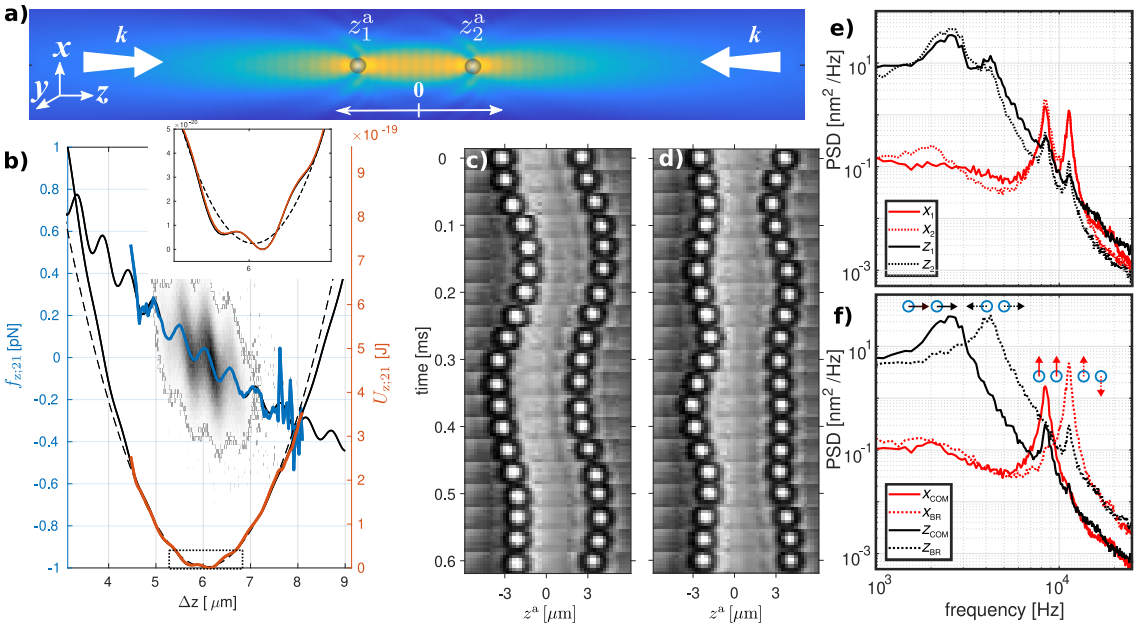

Fig. 4.2: Optical binding of two identical particles confined at a low ambient pressure in cross-polarized, counter-propagating trapping beams. a) Spatial distribution of optical intensity modified by light scattering from the two optically bound silica particles with nominal diameter $d = 600$ nm and refractive index $n = 1.45$, located on the beam axis at $z_1^{\mathrm{a}}, z_2^{\mathrm{a}}$. b) Comparison of the experimental inter-particle force, $f_{\mathrm{z;21}}$ (blue line) and potential, $U_{\mathrm{z;21}}$ (orange line) with their theoretical counterparts (solid black lines of corresponding shapes) plotted as a function of the inter-particle distance, $\Delta z = z_2^{\mathrm{a}} - z_1^{\mathrm{a}}$. For reference, a parabolic fit to the experimental potential is plotted using dashed black line The greyscale-coloured 2D histogram visualizes the full distribution of the experimental inter-particle forces, $m\Delta\ddot{z}(t)$. The inset illustrates a weak sinusoidal modulation of the potential near its minimum. c) Sequence of video frames showing oscillation of the bound particles in the center-of-mass (COM) mode. d) Sequence of video frames showing oscillation of the bound particles in the breathing (BR) mode. e) Experimental power spectral densitites (PSDs) of $(x_1^{\mathrm{a}}, z_1^{\mathrm{a}})$ and $(x_2^{\mathrm{a}}, z_2^{\mathrm{a}})$ determined for individual bound particles 1 and 2. f) Experimental PSDs of $(x_{\mathrm{COM}}, z_{\mathrm{COM}})$ and $(x_{\mathrm{BR}}, z_{\mathrm{BR}})$ determined for COM and BR normal modes. Directions of motion of individual particles in the modes are illustrated by blue circles with arrows. Experimental parameters: $w_0 = 1.95\,\mu$m, $P = 70\,$mW in both beams.

with different relative weights. This notion can be illustrated by the power spectral densities (PSDs) of particle positions calculated from the particle trajectories $[x_1^{\mathrm{a}}(t), z_1^{\mathrm{a}}(t)]$ and $[x_2^{\mathrm{a}}(t), z_2^{\mathrm{a}}(t)]$ recorded in the $x-z$ plane. As shown in Fig. 4.2e), the position PSDs of both particles 1 and 2 along the x and z directions feature distinct

peaks corresponding to $\omega^x_{\mathrm{COM}}/2\pi$ ($\omega^z_{\mathrm{COM}}/2\pi$) and $\omega^x_{\mathrm{BR}}/2\pi$ ($\omega^z_{\mathrm{BR}}/2\pi$). The differences between the transverse (x) and axial (z) values of the mode resonant frequencies stem from the different values of k and b along these two directions [105]. Upon carrying out the coordinate transformations indicated in Eqs. (4.1a) and (4.2b), the two normal modes can be separated, as verified by the PSDs of (x_{COM}, z_{COM}) and (x_{BR}, z_{BR}) plotted in Fig. 4.2f).

The resonant frequency, ω^z_{BR}, of the axial breathing mode reflects the overall optical inter-particle force characterized by the spring constants k of the external optical potential and b of the optical binding interaction (see Eq. (4.2b)). To determine the profile of this force from the experimental data, we first calculated the acceleration of breathing-mode oscillations along the actual mode trajectory, using numerical differentiation of the particle separation distance $\Delta z(t) = [z^{\mathrm{a}}_2(t) - z^{\mathrm{a}}_1(t)]$, and subsequently obtained the averaged net inter-particle force along the z-axis as $f^{\mathrm{net}}_{z;21}(\Delta z) = m\langle \Delta\ddot{z}(t)\rangle_{[\Delta z, \Delta z+\delta z)}$ (the same force estimation principle sa described in Chapter 5). Since the hydrodynamic and thermal forces average out, $f^{\mathrm{net}}_{z;21}(\Delta z)$ directly represents the all-optical axial inter-particle force. Figure 4.2b) compares the experimentally determined inter-particle force, $f^{\mathrm{net}}_{z;21}(\Delta z)$ (blue line), with its theoretical counterpart, $f^{\mathrm{th}}_{\mathrm{z};21}(\Delta z) = (f_{z;2} - f_{z;1})$ (black line), calculated as the difference of the axial optical forces $f_{z;2}$, $f_{z;1}$ acting on the two illuminated, optically bound particles. For the actual experimental values of system parameters, the model based on multiple-scattering Mie theory [110, 106] agrees very well with the experiments. A similar conclusion applies to the experimental (orange line) and theoretical (black line) inter-particle potentials, $U_{\mathrm{z};21}(\Delta z)$, calculated by integration of the corresponding forces as $U_{\mathrm{z};21}(\Delta z) = -\int f_{\mathrm{z};21}(\Delta z)\mathrm{d}\Delta z$.

4.3 Non-linearly coupled particles.

Within the experimentally relevant range of Δz, the axial optical inter-particle potential resembles a harmonic potential well with a superimposed sinusoidal modulation (see the inset in Fig. 4.2b). Consequently, the associated axial optical inter-particle force, $f_{\mathrm{z};21}(\Delta z)$, is:

$$f_{\mathrm{z};21}(\Delta z) = -B(\Delta z - \langle \Delta z\rangle) - \alpha \sin(4\pi[\Delta z - \langle \Delta z\rangle]/\lambda). \tag{4.3}$$

Here, B is the stiffness (spring constant) of the harmonic part of the force and α describes the magnitude of the oscillating optical binding force with a spatial period of $\lambda/2$, arising due to interference of the incident and back-scattered light [106, 111]. Depending on the incident light power, two qualitatively different types of the trapped particles' behaviour can be observed. For low light powers, the depth of the secondary optical traps created due to the sinusoidal modulation of the harmonic

potential background is below the thermal energy k_BT and these traps cannot stably confine the particles subject to stochastic thermal forces. Thus, the modulation has a negligible impact on the particles' axial motion, which is determined primarily by the harmonic part of the inter-particle force associated with the constant stiffness B. In this case, the resonant frequency of the axial breathing mode given by Eq. (4.2b) is $\omega_{\mathrm{BR}}^{z} = \sqrt{(k+2b)/m} = \sqrt{B/m}$. On the other hand, for sufficiently high light powers, the secondary traps deepen and additional stable particle configurations appear at separation distances Δz, for which $f_{\mathrm{z};21}(\Delta z) = 0$ and $(\mathrm{d}f_{\mathrm{z};21}/\mathrm{d}\Delta z) < 0$. Because they are established by both the linear and oscillating part of the axial inter-particle force, these secondary equilibria are characterized by a higher stiffness of confinement. For small deviations from the equilibrium configuration corresponding to $\Delta z = \langle \Delta z \rangle$, the sine term in Eq. (4.3) can be linearised using Taylor series expansion, yielding an effective stiffness,

$$B^{\mathrm{sin}} \approx B + 4\pi\alpha/\lambda, \tag{4.4}$$

which determines the value of $\omega_{\mathrm{BR}}^{z,\mathrm{sin}} = \sqrt{(k+2b^{\mathrm{sin}})/m} = \sqrt{B^{\mathrm{sin}}/m}$. At intermediate light powers, particle confinement in the secondary optical traps is transient and the thermally driven particles can effectively sample the whole multi-stable anharmonic potential landscape. Consequently, particles' motion displays characteristic frequencies corresponding to both B and B^{sin}, reflecting the non-linear character of the net inter-particle force (4.3) (see Section 2B of the Supplementary Information of [109] for details).

The spatial arrangement and motional dynamics of optically trapped and bound particles strongly depend on the distribution of light intensity of the illuminating beams. As illustrated in Fig. 4.3a), inter-particle separation distance can be sensitively and reversibly tuned by changing the beam waist radius w_0 [112]. In the particular experiment illustrated in Fig. 4.3a), the particle separation was varied between 3 and 13 μm by increasing w_0 from 1.3 to 2.5 μm. Experimentally determined optical inter-particle forces, $f_{\mathrm{z};21}(\Delta z)$ (coloured lines), together with the corresponding fits to Eq. (4.3) (black lines), are shown in Fig. 4.3b) for three different values of w_0. The corresponding fitted values of α significantly increase with reduced inter-particle separation distance, indicating the increasing non-linearity of optical binding [106]. Larger modulation amplitudes α then lead to the appearance of multiple stable particle configurations indicated by dotted vertical lines in Fig. 4.3b)-d). Depending on the value of w_0, various anharmonic inter-particles potentials, $U_{\mathrm{z};21}(\Delta z)$, were observed, including double-wells at small inter-particle separations (see yellow line in Fig. 4.3d) and multi-stable potentials for larger separations (see blue line in Fig. 4.3d). Due to weak barriers between the local minima in the potential landscape, the particles frequently jumped between multiple stable

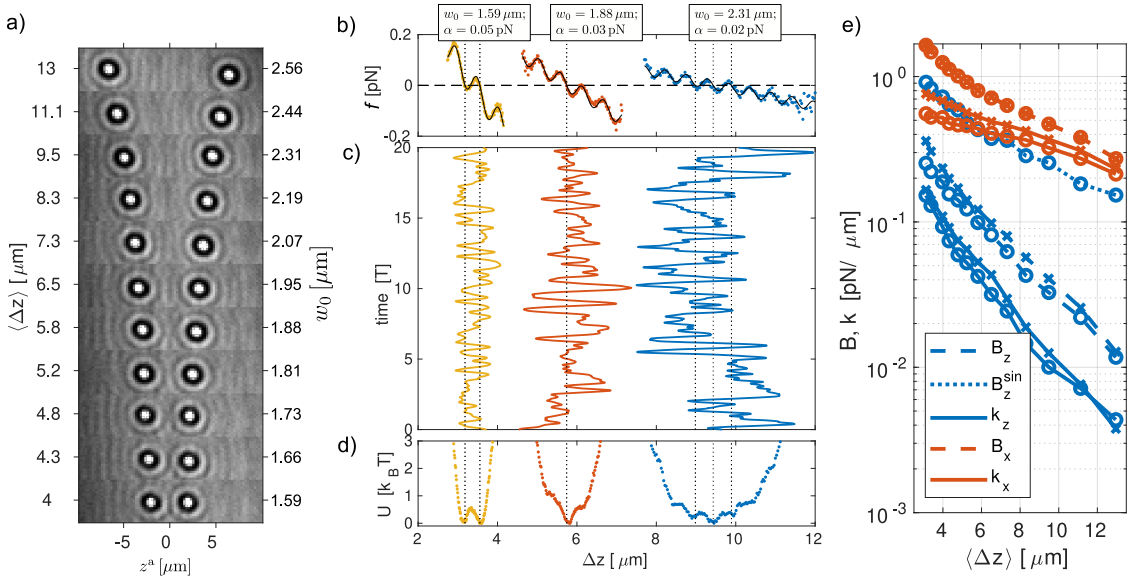

Fig. 4.3: Modification of optically bound structures by adjusting the width of the incident light beams. a) Gradual expansion of an optically bound structure of two particles upon increasing the beam waist radius w_0. b) Experimentally determined axial inter-particle forces, $f_{z;21}$ (coloured lines), together with the fits to Eq. (4.3) (black lines) for different values of $\langle \Delta z \rangle$. c) Time evolution of breathing-mode trajectories along the z-axis. The time is specified in the units of the breathing-mode oscillation period, T. d) Demonstration of anharmonicity of inter-particle potential, $U_{z;21}$, caused by light interference. The potential profiles were determined by integration of the corresponding force profiles, $f_{z;21}$, shown in part b). e) Experimental dependence of the stiffness k_x, k_z of the external trapping potential, harmonic inter-particle stiffness B_x, B_z, and modulated inter-particle stiffness $B_z^{\sin}$ on the mean inter-particle distance $\langle \Delta z \rangle$. Circles ($\circ$) denote the stiffness values determined from the experimental force profiles reconstructed from the recorded particle trajectories, crosses ($\times$) denote the stiffness values obtained from the corresponding resonant mode frequencies using Eqs. (4.1a-4.2b). All the data correspond to ambient pressure 6 millibar and laser power $P = 37$ mW in both beams.

configurations, with a transition rate comparable to $\omega_{\mathrm{BR}}^z/2\pi = \sqrt{B/(4\pi^2 m)}$, see Fig. 4.3c).

Figure 4.3e) compares the stiffness k of the external trapping potential with the harmonic (B) and sinusoidally modulated ($B^{\sin}$) inter-particle stiffness for different mean particle separation distances, $\langle \Delta z \rangle$. Individual stiffness values were found using two independent procedures. In the first one, the stiffness was calculated from the spatial profiles of the inter-particle force ($B, B^{\sin}$) and external trapping force (k) acting on the system of optically bound particles; these force profiles were

determined from the analysis of experimental particle trajectories (see discussion above and in Methods). Alternatively, the stiffness was estimated from the position of the characteristic spectral peaks in the PSDs of normal-mode coordinates and known particle mass (see Methods). As illustrated in Fig. 4.3e), the values of k and B obtained from the two procedures agree very well for both x and z directions. Due to the small oscillation amplitude of particles confined in the secondary optical traps in multi-stable potentials and broadening of spectral peaks caused by anharmonicity of these potentials and relatively large viscous damping, we were not able to observe clear evidence of oscillatory peaks corresponding to $\omega_{\mathrm{BR}}^{z,\mathrm{sin}} = \sqrt{B^{\mathrm{sin}}/m}$ in the modal PSDs.

4.4 Conclusion

In summary, we demonstrated stable optical binding of 2 microscopic silica particles confined in the underdamped regime, at pressures lower than 20 mbar, using cross-polarized counter-propagating Gaussian beams (stable optical binding with up to 4 particles shown in full version of this thesis). We presented a methodology that determines the parameters of such coupled oscillators - in particular, the trapping and binding stiffness - from the camera record of particles' trajectories. We were able to clearly resolve collective vibrational modes of optically bound structures characteristic of linearly coupled harmonic oscillators moving in the presence of weak viscous damping and hydrodynamic coupling. In addition, we observed and characterized sinusoidal modulations of the optical binding potentials describing a weak non-linear inter-particle coupling, which is caused by interference of the incident and back-scattered light [106] and results in multistability of such optically bound matter [111]. Similar type of externally controllable coupling non-linearity could facilitate optically induced entanglement between the trapped mesoscopic particles [113, 114], and is of significant interest for the systematic studies of energy redistribution between coupled non-linear oscillators [115, 116]. Currently, the lowest achievable gas pressure at which stable optically bound structures can be formed and maintained is limited to $\sim$ 1 mbar by heating effects, which substantially increase the centre-of-mass motion of the particles, causing unwanted collisions and instabilities (see full version of this thesis for more details). However, by implementing a parametric feedback cooling scheme [117, 118] or cavity-assisted cooling [36], both recently developed for individual optically levitated nanoparticles, it is feasible to selectively cool the collective vibrational modes of the structures, possibly all the way down to the quantum ground state.

5 Force estimation from stochastic trajectory

The optical forces acting on a probe particles are utilized in broad range of experimental techniques used in soft and active matter, biophotonics or optomechanics. Often, the precise knowledge of the force field felt by the particle is essential. In this chapter I focus on an unresolved method how to extract an acting force from a measured particles stochastic trajectory.

None of the current methods is capable of mapping complex non-conservative force fields using the under-damped stochastic motion of the trapped bead. The calibration techniques used today are either suitable only for certain field geometry or they are limited to the over-damped regime. The methods as potential analysis (PA), equipartition method, mean squared displacement analysis, autocorrelation function analysis (all described in Ref. [119]) or Bayesian inference methods [120, 121, 122, 123] assume harmonic oscillator as the model system. The Bayesian methods as well as maximum likelihood method FORMA [124] or the mean drift method [125, 126, 127] are applicable only on over-damped bead dynamics. Some methods can be used for inference of more complex conservative fields (FORMA or potential analysis [119]). It was even shown that FORMA, ACF or Bayesian inference can be adapted for non-conservative force field measurement [128], but still only for over-damped dynamics. Here we present a powerful algorithm for local force estimation based on calculation of local average velocity and acceleration of Brownian trajectories in under-damped regime. The presented approach estimates correctly both the conservative and the non-conservative fields. The performance of the algorithm is shown using experimentally measured trajectories. In the full version of this thesis the method is demonstrated also on simulated stochastic trajectories and the influence of additive noise in detection of the probe particle position.

I worked out the original idea proposed by my colleague L. Chvátal to the form presented below. I developed the Matlab scripts processing input data, designed the simulations, carried out the experiments and evaluated the performance of the proposed method. I also addressed the influence of additive noise in position detection chain on the estimated force values, came up with the presented correction procedure and implemented it in the Matlab scripts. L. Chvátal helped me with derivation of the joint distribution of noise and the second derivative of noise. The simulation software used for 1D simulations was developed by M. Šiler, the simulations of stochastic motion in 2D non-conservative force fields were provided by Stephen Simpson.

5.1 Estimation procedure

In general, the motion of optically trapped spherical bead is given by a Langevine equation,

$$\mathbf{F}(\mathbf{r}) - \gamma\dot{\mathbf{r}} + \mathbf{F}^{\mathrm{L}}(t) = m\ddot{\mathbf{r}}. \tag{5.1}$$

Here, $\mathbf{F}$ would typically be the optical force as a function of position, $\mathbf{r} = (x, y, z)$. But in general, $\mathbf{F}$ could be any kind of force, which depends only on position. For example, electrostatic force on electrically charged particle or combination of optical and electrostatic force. In any case, the first term in equation (5.1), the force $\mathbf{F}(\mathbf{r})$, is the force we estimate and refer to in this chapter. $\mathbf{F}^L(t)$ is the Brownian stochastic force caused by air molecules randomly impinging on the bead. $\mathbf{F}^L(t)$ is a white-noise process fulfilling:

$$\langle \mathbf{F}^{\mathrm{L}}(t) \rangle = 0 \tag{5.2a}$$

$$\langle \mathbf{F}^{\mathrm{L}}(t) \otimes \mathbf{F}^{\mathrm{L}}(t') \rangle = 2k_{\mathrm{B}}T\gamma\mathbf{I}\delta(t - t'), \tag{5.2b}$$

with $\mathbf{I}$ being the unit matrix. Here we consider only time independent optical forces, $\mathbf{F} \neq \mathbf{F}(t)$. Lets assume a bead is moving along a certain stochastic trajectory $\mathbf{r}(t)$ fulfilling equation (5.1) and we are interested in finding the value of force $\mathbf{F}(\mathbf{r}_0)$ in particular position $\mathbf{r}_0$. During its motion, the bead visits $\mathbf{r}_0$ many times. Every time the beads position is $\mathbf{r} = \mathbf{r}_0$, it feels the same force $\mathbf{F}(\mathbf{r}_0)$, but the viscous drag $\gamma\dot{\mathbf{r}}$ and inertia $m\ddot{\mathbf{r}}$ differ from time to time, since the trajectory is stochastic. Now we average the equation of motion (5.1) only across the time instants, when the beads position is $\mathbf{r}_0$, formally writing

$$\langle \mathbf{F}(\mathbf{r}) \rangle_{\mathbf{r}=\mathbf{r}_0} - \gamma\langle \dot{\mathbf{r}} \rangle_{\mathbf{r}=\mathbf{r}_0} + \langle \mathbf{F}^{\mathrm{L}} \rangle_{\mathbf{r}=\mathbf{r}_0} = m\langle \ddot{\mathbf{r}} \rangle_{\mathbf{r}=\mathbf{r}_0}. \tag{5.3}$$

The proposed method assumes, that the Brownian force averages out, $\langle \mathbf{F}^{\mathrm{L}} \rangle_{\mathbf{r}=\mathbf{r}_0} = 0$, for all $\mathbf{r}_0$ and the force is then given by the average velocity and the average acceleration in $\mathbf{r}_0$:

$$\mathbf{F}(\mathbf{r}_0) = \gamma\langle \dot{\mathbf{r}} \rangle_{\mathbf{r}=\mathbf{r}_0} + m\langle \ddot{\mathbf{r}} \rangle_{\mathbf{r}=\mathbf{r}_0}. \tag{5.4}$$

Although a rigorous mathematical proof of this assumption is lacking, in the following text we show that it is reasonable and we rightly estimate the force using equation (5.4).

A typical measured trajectory $\mathbf{r}_n = (x_n, y_n, z_n) = \mathbf{r}(t_n)$ is a series of $\mathcal{N}$ positions in discrete time instants t_n separated by Δt. The velocity $\mathbf{v}_n = \mathbf{v}(t_n)$ and acceleration $\mathbf{a}_n = \mathbf{a}(t_n)$ waveforms are calculated from the measured trajectory $\mathbf{r}_n$ by numerical differentiation using central formulas, two-point formula for velocity and

three-point formula for acceleration.

$$\begin{aligned} \mathbf{v}_n &= \frac{\mathbf{r}_{n+1} - \mathbf{r}_{n-1}}{2\Delta t} \\ \mathbf{a}_n &= \frac{\mathbf{r}_{n+1} - 2\mathbf{r}_n + \mathbf{r}_{n-1}}{\Delta t^2}. \end{aligned} \tag{5.5}$$

The proposed method uses the measured trajectory and calculated velocity and acceleration to estimate the force field not as a continuous function of position $\mathbf{r}$, but in discrete positions using a spatial binning process. The optical trap volume is divided into rectangular spatial boxes of dimensions $\Delta x, \Delta y, \Delta z$ centered around position $\mathbf{b}_i = (b_{x,i}, b_{y,i}, b_{z,i})$. For each box, one value of force $\langle \mathbf{F} \rangle_i$ is calculated by taking the mean value of acceleration and velocity, but the mean value is taken only across the time instants when the bead is positioned inside the particular bin $\mathbf{b}_i$ - this is the averaging operation we indicate by $\langle \cdot \rangle_i$ and defined by equations (5.6) and (5.7). This is illustrated in Fig. 5.1a where a little section of a stochastic trajectory is plotted. The red dashed lines show the edges of bin b_{13}, the samples that are taken into the mean values calculated for b_{13} are plotted in red. From now on, the subscript n refers to a particular time instants (or samples) in time (t_n), whereas the subscript i refers to particular spatial bin.

The mean velocity and acceleration in a bin $\mathbf{b}_i$ is calculated as follows:

$$\langle \mathbf{a} \rangle_i = \frac{1}{\mathcal{N}_i} \sum_{n=1}^{\mathcal{N}} \mathbf{a}_n I(\mathbf{b}_i, \mathbf{r}_n) \tag{5.6a}$$

$$\langle \mathbf{v} \rangle_i = \frac{1}{\mathcal{N}_i} \sum_{n=1}^{\mathcal{N}} \mathbf{v}_n I(\mathbf{b}_i, \mathbf{r}_n) \tag{5.6b}$$

$$\langle \mathbf{r} \rangle_i = \frac{1}{\mathcal{N}_i} \sum_{n=1}^{\mathcal{N}} \mathbf{r}_n I(\mathbf{b}_i, \mathbf{r}_n), \tag{5.6c}$$

where $I(\mathbf{b}_i, \mathbf{r}_n) = 1$, if the beads position $\mathbf{r}_n$ in time t_n is within the spatial bin $\mathbf{b}_i$ (red samples for b_{13} in Fig. 5.1a), otherwise $I(\mathbf{b}_i, \mathbf{r}_n) = 0$. $\mathcal{N}_i = \sum_{n=1}^{\mathcal{N}} I(\mathbf{b}_i, \mathbf{r}_n)$ is the total number of points in the bin $\mathbf{b}_i$. The optical force profile is then estimated in discrete positions

$$\langle \mathbf{F} \rangle_i = m \langle \mathbf{a} \rangle_i + \gamma \langle \mathbf{v} \rangle_i. \tag{5.7}$$

The spatial dimensions of position bins are chosen with respect to the force spatial changes. A suitable choice is such that the force change across a bin can be well approximated by linear function. If the force is not constant across a bin, the equations (5.3) and (5.6) do not provide a force estimate centered in $\mathbf{b}_i$. In the following section we show for 1D case that force value found by averaging, $\langle \mathbf{F} \rangle_i$, corresponds to the force value in the mean position $\langle \mathbf{r} \rangle_i$, $\mathbf{F}(\langle \mathbf{r} \rangle_i)$, rather than to the force value in the center of the bin $\mathbf{F}(\mathbf{b}_i)$ due to the irregular position probability

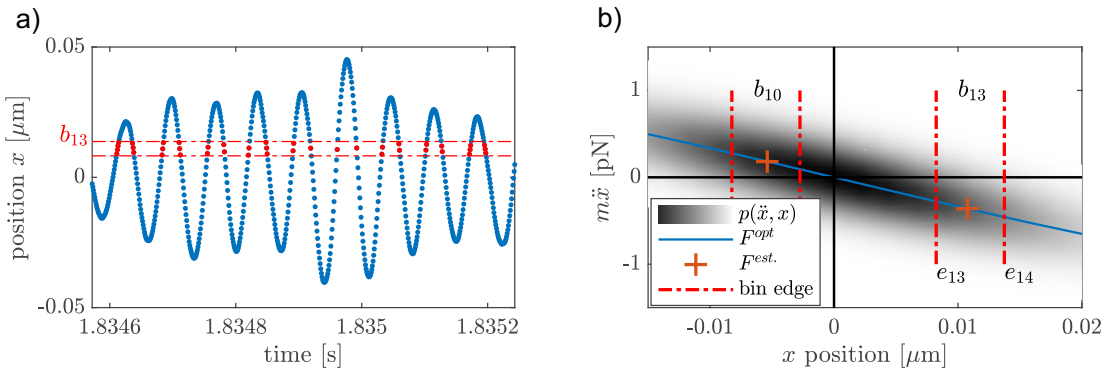

Fig. 5.1: Illustration of the binning principle, where $\mathbf{r} = (x_n)$ and $\mathbf{b}_i = (b_{x,i})$. (a) While calculating the mean values for bin b_{13} only the time instants when the position is inside the bin (red samples) are taken into account. (b) The grayscale map is the 2D histogram of the bead having the position x and acceleration $\ddot{x}$ (multiplied by mass m). When estimating the mean force $\langle F \rangle_i$ (orange cross), the acceleration is averaged across the area between the respective bin edges. The blue curve is the original force profile $F(x)$ which is searched for. In 1D case the mean velocity is zero and does not contribute to the mean force as discussed later.

density function within the bin. This means, that the method does not provide estimates of force value in regularly spaced positions $\mathbf{b}_i$, but in irregularly spaced mean positions in bins, $\langle \mathbf{r} \rangle_i$, defined by eq. (5.6c).

We would like to stress several aspects of the binning method:

- we estimate the uncertainty $u(\langle Q \rangle_i)$ of mean values of quantity Q (force, velocity, acceleration) as the standard deviation of the mean. This uncertainty decreases as $1/\sqrt{\mathcal{N}_i}$ so the precision of estimation grows with number of samples in each bin. The estimated force value in bins which are visited very rarely can be quite high.
- the method provides reasonable estimation for position dependent forces only. We suspect our method would fail in case the force is also dependent on time or orientation of the trapped bead, although we have not investigated these cases properly. For example, in the case of spherically non-symmetrical beads, like discs or nano-wires, where $\mathbf{F}(\mathbf{r})$ is also a function of orientation, this formula would give rather random number. The same would hold for force fields generated by laser beams with unstable, fluctuating optical power or if oscillating external electric force is used for driving the motion of electrically charged bead.
- the bead mass m and drag coefficient γ must be known for precise estimation. Both these parameters can be calculated theoretically from bead size and

density stated by the manufacturer. But the uncertainty of the size stated can be as high as 12% which causes uncertainty about 36% for m and 23% for γ for our typical conditions. The beads parameters can be more precisely measured experimentally. The damping coefficient γ can be estimated with uncertainty easily below 0.1% by fitting the power spectral density function (PSD) of position or the position auto-correlation function of motion in the parabolic potential. The beads mass m can be measured by fitting the beads relaxation to equilibrium position after it was displaced from it by DC electric field [129]. Another method of measuring m is to fit the PSD of motion of electrically charged bead driven by electric field on a single harmonic frequency [130].

- the validity of equation (5.3) requires the mechanical system to be in a steady state so that the mean values do not change in time. It does not require the system to meet additional conditions like conservativness of the force field, thermal equilibrium or at least a state close to thermal equilibrium, so a method of force estimation based on this equation is very universal and reliable, even if the motional state is not precisely known.

5.2 Conservative force field - 1D case

Here we focus on the one-dimensional geometry. Our goal is to estimate the force $\mathbf{F}(\mathbf{r})$ as stated in equation (5.1). For 1D case we use the notation $\mathbf{r} \to x$ and $\mathbf{F}(\mathbf{r}) \to F(x)$. For conservative force field, we assume $\langle v \rangle_i =$ and the force $F(x)$ is given only by mean acceleration (for more details on this assumption see the full version of this thesis).

We show the performance of the method on experimental data. We use the stochastic trajectory of a silica bead trapped in counterpropagating beams (experiment described in section 2). For the trap parameters used, the motion of the bead is well described as harmonic oscillator and the force is linear function of x. Note that in the linear case the force function can be determined from knowledge of the oscillators mass m and the natural frequency Ω_0 as $F = -m\Omega_0^2 x$. The binning method offers no advantage for the linear case since the natural frequency can be found by fitting the theoretical PSD function S_{xx} into the measured one and the mass needs to be known anyway. But the linear case offers the opportunity to verify the binning method even without the precise knowledge of the beads mass or even without precisely calibrated position measurement.

First, from the measured trajectory the natural frequency is determined. If the mass is not known, the binning method gives the average acceleration experienced

by the bead passing certain bin (see Fig. 5.2):

$$\langle a_x \rangle_i = \Omega_0^2 \langle x \rangle_i, \tag{5.8}$$

with the slope corresponding to the natural frequency squared determined from PSD fitting [131].

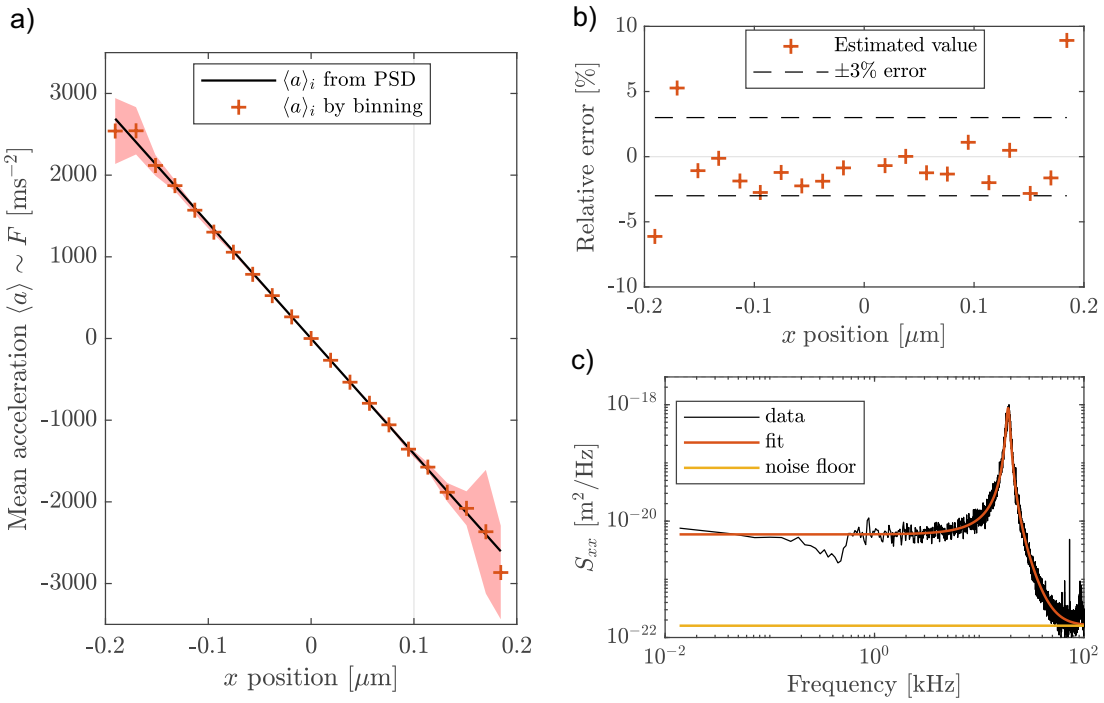

Fig. 5.2: Binning method performance on 1D experimental data. The trapping power was 175 mW and the motion was captured by videomicroscopy using fast camera with framerate of 200 000 fps. The recording was 0.7 s long and contained 138000 frames. The stochastic trajectory was tracked from the video recording by fitting 2D Gaussian distribution into the image of the trapped bead. The natural frequency of the oscillator Ω_0 was found by fitting the one-sided Power Spectral Density (PSD) S_{xx} by the theoretical function as described in Chapter 3, Supplementary note 5 (see Fig. 5.2c)). Since the mass is not known, only the mean accelerations are plotted. (a) Black line - mean acceleration as suggested by the measured natural frequency of the oscillator. Orange crosses - mean accelerations estimated by binning. (b) Relative error of estimation. (c) One sided PSD function. Black curve - data. Red curve - theoretical fit. Yellow curve - position measurement noise floor.

Here we show the performance of our method by comparing the mean acceleration determined by binning and determined by fitting the PSD. We used one of the measurements of particles motion in standing wave of counter-propagating beams

published in our previous paper [91] (Chapter 3). The obtained value $\frac{\Omega_0}{2\pi} = 18.9$ kHz was used for construction of the expected mean acceleration function $\langle a_x \rangle = -\Omega_0^2 x$ which is plotted as the black line in Fig. 5.2a). The mean acceleration values obtained by binning are depicted in Fig. 5.2a) by orange crosses and the coincidence with the expected values is very good. The light red area in the figure represents the uncertainty of the estimated value defined by $\langle a_x \rangle \pm \sigma$ with σ being the standard error of the mean calculated across the respective bin samples. As shown in Fig. 5.2b), the relative error is as small as 3% for majority of the bins. The error gets higher only for the outer bins, where the number of samples taking part in the averaging is very low (typically units of samples) and the uncertainty is high. Still, even though the statistics is so poor for these bins, the relative error is less than 10%. In this case, the precision of force measurement would be limited mainly by the precision of position detection calibration and the precision of knowledge of mass m.

5.3 Non-conservative force field - 2D case

The force field generated by optical trap can be in general non-conservative, for example due to the intrinsic properties of optical tweezers or bad alignment of a trap. A non-conservative force field can also be introduced on purpose by design of the trap itself in order to generate and study the non-equilibrium dynamics of the trapped bead. In either case, it is useful to have a method for characterization of the resulting force $\mathbf{F}(\mathbf{r})$, as introduced in eq. (5.1).

If a particle is subjected to a non-conservative force field, in general it does not reach thermal equilibrium with the surrounding gas. Instead it can reach a steady state, but this state is not described by the Gibbs-Boltzmann distribution anymore. It follows that mean velocity across one bin $\langle \mathbf{v} \rangle_i$ does not need to be zero and the full version of equation (5.7) must be used. So if the force is estimated in 2D grid of bins $\mathbf{b}_i = (b_{x,i}, b_y, i)$, the estimated force becomes

$$\langle \mathbf{F} \rangle_i = \langle \mathbf{F} \rangle_i^{acc} + \langle \mathbf{F} \rangle_i^{vel} \tag{5.9}$$

with $\langle \mathbf{F} \rangle_i^{acc} = m \langle \mathbf{a} \rangle_i$ being the mean acceleration part and $\langle \mathbf{F} \rangle_i^{vel} = \gamma \langle \mathbf{v} \rangle_i$ the mean velocity part.

We have shown experimentally in our recent publication [91] that such out of equilibrium steady state can be reached in optical trap formed by circularly polarized counter-propagating beams in low pressure. In such trap the force field is composed of strong radial component F_ρ generated by gradient forces and much weaker azimuthal component F_ϕ generated mainly by spin force, which is connected to the circular polarization. The total force field have cylindrical symmetry.

In order to show the performance of the method on experimental data we applied it on the measurements published in [91] and compared the force obtained by binning to the force published in the paper in Fig. 3c.

The optical force field was estimated in the following manner:

1. calculate the 2D force field in 2D rectangular mesh of bins for each trajectory separately, the position bins are the same for all trajectories. For each trajectory some bins remain blank since they are not visited by the bead
2. decompose the force field into radial $\mathbf{F}_i^{\rho}(\rho)$ and azimuthal $\mathbf{F}_i^{\phi}(\rho)$ component
3. calculate the radial $F_\rho(\rho)$ and azimuthal $F_\phi(\rho)$ component as a function of only radial position ρ by averaging across all bins, whose radial distance from trap center is in the interval $(\rho; \rho + \mathrm{d}\rho)$
4. divide the force components by the corresponding trapping power P to get the normalized optical force $f = F/P$
5. average $f_\rho(\rho)$ and $f_\phi(\rho)$ to get the final normalized force components

Although the force field should be centrally symmetric, the estimated field is rather deformed. Which is expected since the observed orbital trajectories are not precisely circular and shows that the method is capable of mapping the real field instead of relying on some parametric approximate model. When we choose certain radial distance ρ from the trap axis the distribution of magnitude of the force components is quite broad for that ρ because of the force field asymmetry (see Fig. 5.3c,d). Nevertheless, taking the average values across the azimuthal coordinate produces the average radial force profile very similar to that shown in Chapter 3. In Fig. 5.3f, there is the estimated azimuthal component (circles) which fits nicely the profile (solid black curve) taken from Ref.[91]. We also fit the radial and azimuthal components by linear function for small radial displacement and express it in terms of radial stiffness k_ρ and azimuthal stiffness k_ϕ and compare it to the values presented in Chapter 3 (see Tab. 5.1). The stiffnesses obtained by binning are very similar to those previously published, they only differ by units of percent.

Quantity	Binning	NatComm
k_ϕ [N/Wm]	3.17×10^{-5}	3.30×10^{-5}
k_ρ [N/Wm]	2.22×10^{-4}	2.38×10^{-4}
k_ρ/k_ϕ	0.146	0.138

Tab. 5.1: Comparison of stiffnesses obtained by binning method and those published in Ref. [91] (see Chapter 3).

In conclusion, the binning method provides correct force field estimate even for the non-conservative case as proved on 2D simulated trajectories. It proved itself

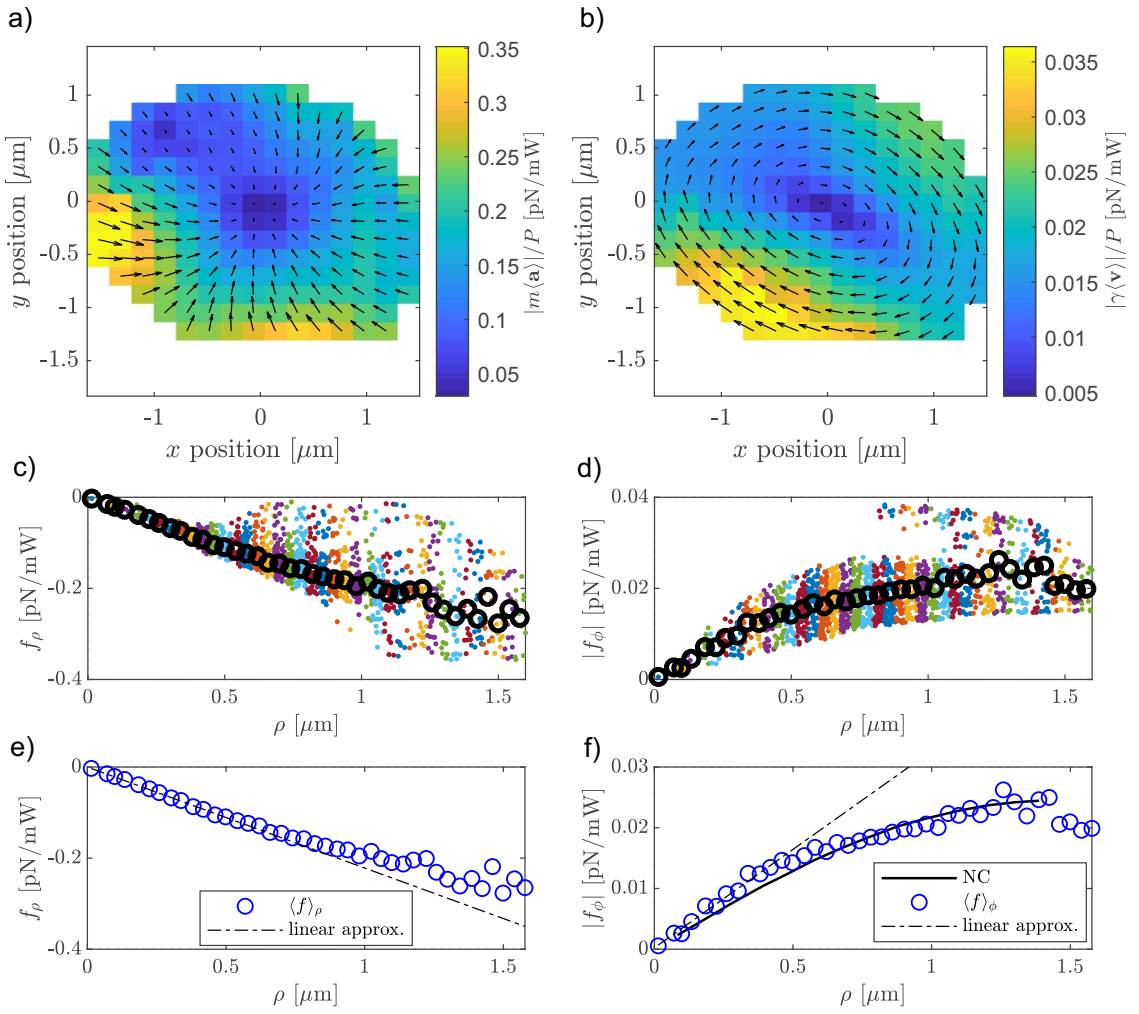

Fig. 5.3: Non-conservative force field estimation from experimental stochastic trajectories. (a) Mean acceleration component. (b) Mean velocity component. (c) Radial component of total force. The different color of datapoints indicate the different azimuthal positions across which the mean force $f_\rho(r)$ (circles) is calculated. (d) Azimuthal component of total force. The color encoding is the same as in (c). (e) Estimated radial profile of the force field - radial component. (f) Estimated radial profile of the force field - azimuthal component. NC stands for data published in [91].

also on experimental data where it reproduced the force field determined beforehand by different method. The presented binning method seems to fill the gap among the force measurement methods as listed in the beginning of this chapter.

5.4 Summary

In this chapter we introduced a powerful method for characterization of optical trap force fields acting on a probe particle. The method is based on analysis of the measured particles stochastic trajectory. Unlike other approaches, it does not assume special force field shape, conservativeness, thermal equilibrium steady state or certain temperature of the surrounding gas. The only assumption is under-damped dynamics of the trapped bead and knowledge of its mass and drag coefficient, thus making it ideal tool for characterization of optical traps in low pressure environment. The good performance of the proposed method was shown on experimental stochastic trajectories, the performance on simulated numerically simulated trajectories is discussed in full version of this thesis, where also the effect of additive noise in position measurement is investigated.

6 Conclusion

The presented doctoral thesis reports on development of experimental apparatus for optical trapping experiments at low pressure. Lowering the pressure enables us to reach under-damped regime of motion, control the stochastic forces acting on the particle or even minimize the coupling of the motion to the surrounding to the extent that quantum ground state of motion can be reached. Precisely engineering and controling the optical trap allows to prepare and control out of equilibrium steady states of motion, making optical levitation suitable testbed for test of nonequilibrium thermodynamics. Levitated optomechanics is therefore very rapidly developing platform promising exciting discoveries not only in terms of fundamental questions classical and quantum physics, but mainly in terms of the transition between of those two. We believe the work presented in this thesis not only laid the foundations of experimental levitated optomechanics in the Institute of Scientific Instruments of the CAS, v.v.i., but also contributed experimentally to research of such phenomena as spin-force generated non-equilibrium states or optical binding in under-damped regime.

Since trapping in vacuum has never been realised before at the Institute of Scientific Instruments of the CAS, new optical trap and other necessary experimental methods such as optical setup adjustment, particle loading into the vacuum optical trap and tracking had to be developed. Chapter 2 shows how these issues were dealt with. We chose to implement dual-beam optical trap geometry due to its versatility. In the experiment we incorporated two particle position detection schemes - QPD detection and videomicroscopy. QPD provides us with real-time information of the position in 3D but it can be used for tracking only one particle. Also the determination of the calibration factor transforming the position signal from volts to meters is rather treacherous. Videomicroscopy on the other hand is able to capture position of several objects and the calibration is straightforward, but the information is extracted after measurement by postprocessing. Regarding the particle loading problem, two techniques were successfully developed. First technique uses an ultrasonic nebuliser for spraying little liquid droplets containing one particle into the trap under atmospheric conditions. Second technique, laser induced desorption, uses laser pulses to catapult particles from silicon wafer into the trap under vacuum conditions.

Chapter 3 presents our experimental observation of an optical force acting on trapped particle perpendicularly to light propagation direction which is generated by non-zero spin angular momentum of the optical field. The effect was shown by comparing the dynamics of probe particle trapped in linearly polarised (zero spin) and circularly polarised (maximal spin) light. We showed that spin force makes the

trapping force field non-conservative, it biases Brownian motion and drives it out of equilibrium. If the spin force is big enough, it induces orbital motion around optical axis and ultimately throws the probe particle from an optical trap.

Optical force fields are generally non-conservative, and their structure is derived from internal momentum flows. Measuring the trajectories of probe particles in vacuum can help us develop our understanding of optical momentum flows in structured light fields as well as the dynamics and thermodynamics associated with motion in potentially complex force fields. Some of these possibilities have previously been described by Berry and Shukla [94, 95].

Chapter 4 summarizes our recent effort in the field of optical binding. We successfully trapped two silica microspheres in free space dual-beam optical trap in vacuum, which is, to our knowledge, experimental arrangement never used before. In the under-damped motion of the trapped spheres we observed clear mode splitting proving the binding interaction between the particle. We also observed collisions of the spheres at pressures around 1 mbar suggesting that for reaching lower pressures, active feedback stabilization will be needed. Finally we introduced a method for characterization of the binding force based on calculation of local mean second derivative of the mode coordinate.

In chapter 5 the idea of binding force calculation was generalized to a method capable of calculating arbitrary optical force field using just the probe particles under-damped stochastic trajectory, mass and damping coefficient. We showed the performance of the method on both numerically simulated and experimental data. Although we admit that the method would need some mathematical polishing and detailed estimation error analysis, we believe that it can be useful tool for optical trap calibration, quality evaluation. For example, experiments studying thermodynamics could profit from this method since the work done along some trajectory is calculated from the knowledge of the local force.

Bibliography

1. ASHKIN, A. Acceleration and Trapping of Particles by Radiation Pressure. *Phys. Rev. Lett.* 1970, **24**, 156–159.
2. MCGLOIN, D. Optical tweezers:20 years on. *Phil. Trans. R. Soc. A*. 2006, **364**, 3521–3537.
3. LANG, M. J.; BLOCK, S. M. Resource letter: LBOT-1: Laser-based optical tweezers. *Am. J. Phys.* 2003, **71**, 201–215.
4. MEHTA, A. D.; RIEF, M.; SPUDICH, J. A.; SMITH, D. A.; SIMMONS, R. M. Single-molecule biomechanics with optical methods. *Science*. 1999, **283**, 1689–1695.
5. BUSTAMANTE, C.; BRYANT, Z.; SMITH, S. B. Ten years of tension: single-molecule DNA mechanics. *Nature*. 2003, **421**, 423–427.
6. ASHKIN, A.; DZIEDZIC, J. M.; BJORKHOLM, J. E.; CHU, S. Observation of a single-beam gradient force optical trap for dielectric particles. *Opt. Lett.* 1986, **11**, 288–290.
7. GRIER, DG; ROICHMAN, Y. Holographic optical trapping. *Appl. Opt.* 2006, **45**(5), 880–887.
8. VISSCHER, K.; GROSS, S. P.; BLOCK, S. M. Construction of multiple-beam optical traps with nanometer-resolution position sensing. *IEEE J. Sel. Top. Quantum Electron.* 1996, **2**, 1066–1076.
9. BURNS, M. M.; FOURNIER, J.-M.; GOLOVCHENKO, J. A. Optical Matter: Crystallization and Binding in Intense Optical Fields. *Science*. 1990, **249**, 749.
10. CHIOU, A. E.; WANG, W.; SONEK, G. J.; HONG, J.; BERNS, M. W. Interferometric optical tweezers. *Opt. Commun.* 1997, **133**, 7–10.
11. CASABURI, A.; PESCE, G.; ZEMÁNEK, P.; SASSO, A. Two-and three-beam interferometric optical tweezers. *Opt. Commun.* 2005, **251**, 393–404.
12. ZEMÁNEK, P.; JONÁŠ, A.; ŠRÁMEK, L.; LIŠKA, M. Optical trapping of Rayleigh particles using a Gaussian standing wave. *Opt. Commun.* 1998, **151**, 273–285.
13. ZEMÁNEK, P.; JONÁŠ, A.; ŠRÁMEK, L.; LIŠKA, M. Optical trapping of nanoparticles and microparticles using Gaussian standing wave. *Opt. Lett.* 1999, **24**, 1448–1450.
14. ČIŽMÁR, T.; GARCÉS-CHÁVEZ, V.; DHOLAKIA, K.; ZEMÁNEK, P. Optical conveyor belt for delivery of submicron objects. *Appl. Phys. Lett.* 2005, **86**, 174101.

15. ČIŽMÁR, T.; ŠILER, M.; ZEMÁNEK, P. An optical nanotrap array movable over a milimetre range. *Appl. Phys. B.* 2006, **84**, 197–203.

16. KORDA, P. T.; TAYLOR, M. B.; GRIER, D. G. Kinetically locked-in colloidal transport in an array of optical tweezers. *Phys. Rev. Lett.* 2002, **89**, 128301.

17. MACDONALD, M. P.; SPALDING, G. C.; DHOLAKIA, K. Microfluidic sorting in an optical lattice. *Nature.* 2003, **426**, 421–424.

18. DHOLAKIA, K.; MACDONALD, M. P.; ZEMÁNEK, P.; ČIŽMÁR, T. Cellular and colloidal separation using optical forces. *Methods in Cell Biology.* 2007, **82**, 467–495.

19. ASHKIN, A.; DZIEDZIC, J. M. Optical levitation by radiation pressure. *Appl. Phys. Lett.* 1971, **19**, 283–285.

20. MCGLOIN, D.; BURNHAM, D. R.; SUMMERS, M. D.; RUDD, D.; DEWAR, N.; ANAND, S. Optical manipulation of airborne particles: techniques and applications. *Faraday Discuss.* 2008, **137**, 335–350.

21. BURNHAM, D. R.; MCGLOIN, D. Holographic optical trapping of aerosol droplets. *Opt. Express.* 2006, **14**, 4176.

22. SUMMERS, M. D.; BURNHAM, D. R.; MCGLOIN, D. Trapping solid aerosols with optical tweezers: A comparision between gas and liquid phase optical traps. *Opt. Express.* 2008, **16**, 7739.

23. MITCHEM, L.; HOPKINS, R. J.; BUAJARERN, J.; WARD, A. D.; REID, J. P. Comparative measurements of aerosol droplet growth. *Chem. Phys. Lett.* 2006, **432**, 362–366.

24. KING, Martin D.; THOMPSON, Katherine C.; WARD, Andrew D.; PFRANG, Christian; HUGHES, Brian R. Oxidation of biogenic and water-soluble compounds in aqueous and organic aerosol droplets by ozone: a kinetic and product analysis approach using laser Raman tweezers. *Faraday Discuss.* 2008, **137**, 173–192. ISSN 1364-5498.

25. MITCHEM, L.; REID, J. P. Optical manipulation and characterisation of aerosol particles using a single-beam gradient force optical trap. *Chem. Soc. Rev.* 2008, **37**, 756–769.

26. ROOSEN, G.; IMBERT, C. Optical levitation by means of two horizontal laser beams: a theoretical and experimental study. *Phys. Lett.* 1976, **59A**, 6–8.

27. ROOSEN, G. A theoretical and experimental study of the stable equilibrium positions of spheres levitated by two horizontal laser beams. *Opt. Commun.* 1977, **21**, 189–194.

28. TAJI, K.; TACHIKAWA, M.; NAGASHIMA, K. Laser trapping of ice crystals. *Appl. Phys. Lett.* 2006, **88**, 141111.

29. PASTEL, R; STRUTHERS, A; RINGLE, R; ROGERS, J; ROHDE, C; GEISER, P. Laser trapping of microscopic particles for undergraduate experiments. *Am. J. Phys.* 2000, **68**(11), 993–1001. ISSN 0002-9505.

30. GUILLON, M.; MOINE, O.; STOUT, B. Longitudinal optical binding of high optical contrast microdroplets in air. *Phys. Rev. Lett.* 2006, **96**, 143902.

31. MILLEN, J.; DEESUWAN, T.; BARKER, P.; ANDERS, J. Nanoscale temperature measurements using non-equilibrium Brownian dynamics of a levitated nanosphere. *Nature Nanotechnology*. 2014, **9**, 425 EP –.

32. FRIMMER, Martin; GIESELER, Jan; IHN, Thomas; NOVOTNY, Lukas. Levitated nanoparticle as a classical two-level atom. *J. Opt. Soc. Am. B.* 2017, **34**(6), C52–C57.

33. RASHID, Muddassar; TUFARELLI, Tommaso; BATEMAN, James; VOVROSH, Jamie; HEMPSTON, David; KIM, M. S.; ULBRICHT, Hendrik. Experimental Realization of a Thermal Squeezed State of Levitated Optomechanics. *Phys. Rev. Lett.* 2016, **117**, 273601.

34. LI, Tongcang; KHEIFETS, Simon; RAIZEN, Mark G. Millikelvin cooling of an optically trapped microsphere in vacuum. *Nat. Phys.* 2011, **7**(7), 527–530.

35. GIESELER, Jan; DEUTSCH, Bradley; QUIDANT, Romain; NOVOTNY, Lukas. Subkelvin Parametric Feedback Cooling of a Laser-Trapped Nanoparticle. *Phys. Rev. Lett.* 2012, **109**(10).

36. DELIĆ, Uroš; REISENBAUER, Manuel; DARE, Kahan; GRASS, David; VULETIĆ, Vladan; KIESEL, Nikolai; ASPELMEYER, Markus. Cooling of a levitated nanoparticle to the motional quantum ground state. *Science*. 2020, **367**(6480), 892–895. Available from DOI: 10.1126/science.aba3993.

37. MAGRINI, Lorenzo; ROSENZWEIG, Philipp; BACH, Constanze; DEUTSCHMANN-OLEK, Andreas; HOFER, Sebastian G.; HONG, Sungkun; KIESEL, Nikolai; KUGI, Andreas; ASPELMEYER, Markus. Real-time optimal quantum control of mechanical motion at room temperature. *Nature*. 2021, **595**(7867), 373–377.

38. HOANG, Thai M.; MA, Yue; AHN, Jonghoon; BANG, Jaehoon; ROBICHEAUX, F.; YIN, Zhang-Qi; LI, Tongcang. Torsional Optomechanics of a Levitated Nonspherical Nanoparticle. *Phys. Rev. Lett.* 2016, **117**, 123604.

39. KUHN, Stefan; KOSLOFF, Alon; STICKLER, Benjamin A.; PATOLSKY, Fernando; HORNBERGER, Klaus; ARNDT, Markus; MILLEN, James. Full rotational control of levitated silicon nanorods. *Optica*. 2017, **4**(3), 356–360.

40. REIMANN, René; DODERER, Michael; HEBESTREIT, Erik; DIEHL, Rozenn; FRIMMER, Martin; WINDEY, Dominik; TEBBENJOHANNS, Felix; NOVOTNY, Lukas. GHz Rotation of an Optically Trapped Nanoparticle in Vacuum. *Phys. Rev. Lett.* 2018, **121**, 033602.

41. GIESELER, Jan; NOVOTNY, Lukas; QUIDANT, Romain. Thermal nonlinearities in a nanomechanical oscillator. *Nature Physics*. 2013, **9**, 806 EP –. Article.

42. RICCI, F.; RICA, R. A.; SPASENOVIC, M.; GIESELER, J.; RONDIN, L.; NOVOTNY, L.; QUIDANT, R. Optically levitated nanoparticle as a model system for stochastic bistable dynamics. *Nature Communications*. 2017, **8**, 15141. Article.

43. ASPELMEYER, Markus; KIPPENBERG, Tobias J.; MARQUARDT, Florian. Cavity optomechanics. *Reviews of Modern Physics*. 2014, **86**, 1391–1452.

44. ROMERO-ISART, Oriol; JUAN, Mathieu L; QUIDANT, Romain; CIRAC, J Ignacio. Toward quantum superposition of living organisms. *New Journal of Physics*. 2010, **12**(3), 033015.

45. ROMERO-ISART, O.; PFLANZER, A. C.; JUAN, M. L.; QUIDANT, R.; KIESEL, N.; ASPELMEYER, M.; CIRAC, J. I. Optically levitating dielectrics in the quantum regime: Theory and protocols. *Phys. Rev. A*. 2011, **83**, 013803.

46. RANJIT, Gambhir; CUNNINGHAM, Mark; CASEY, Kirsten; GERACI, Andrew A. Zeptonewton force sensing with nanospheres in an optical lattice. *Phys. Rev. A*. 2016, **93**, 053801.

47. XU, Zhujing; LI, Tongcang. Detecting Casimir torque with an optically levitated nanorod. *Phys. Rev. A*. 2017, **96**, 033843.

48. HOANG, Thai M.; PAN, Rui; AHN, Jonghoon; BANG, Jaehoon; QUAN, H. T.; LI, Tongcang. Experimental Test of the Differential Fluctuation Theorem and a Generalized Jarzynski Equality for Arbitrary Initial States. *Phys. Rev. Lett.* 2018, **120**, 080602.

49. BÉRUT, Antoine; ARAKELYAN, Artak; PETROSYAN, Artyom; CILIBERTO, Sergio; DILLENSCHNEIDER, Raoul; LUTZ, Eric. Experimental verification of Landauer's principle linking information and thermodynamics. *Nature*. 2012, **483**(7388), 187–189.

50. SCHMIEDL, T.; SEIFERT, U. Efficiency at maximum power: An analytically solvable model for stochastic heat engines. *EPL (Europhysics Letters)*. 2007, **81**(2), 20003.

51. DHOLAKIA, Kishan; ZEMÁNEK, Pavel. Colloquium: Gripped by light: Optical binding. *Reviews of modern physics*. 2010, **82**(2), 1767.

52. ARNDT, Markus; HORNBERGER, Klaus. Testing the limits of quantum mechanical superpositions. *Nature Physics*. 2014, **10**(4), 271–277. ISSN 1745-2481.

53. ASHKIN, A.; DZIEDZIC, J. M.; BJORKHOLM, J. E.; CHU, S. Observation of a Single-Beam Gradient Force Optical Trap for Dielectric Particles. *Opt. Lett.* 1986, **11**(5), 288–290.

54. HARADA, Y.; ASAKURA, T. Radiation forces on a dielectric sphere in the Rayleigh scattering regime. *Opt. Commun.* 1996, **124**, 529–541.

55. ASHKIN, A.; DZIEDZIC, J. M. Optical Levitation by Radiation Pressure. *Appl. Phys. Lett.* 1971, **19**(8), 283.

56. ASHKIN, A.; DZIEDZIC, J. M.; BJORKHOLM, J. E.; CHU, Steven. Observation of a single-beam gradient force optical trap for dielectric particles. *Opt. Lett.* 1986, **11**(5), 288–290.

57. ROOSEN, G.; IMBERT, C. Optical levitation by means of two horizontal laser beams: A theoretical and experimental study. *Physics Letters A*. 1976, **59**(1), 6 –8.

58. ZEMÁNEK, Pavel; JONÁŠ, Alexandr; ŠRÁMEK, Libor; LIŠKA, Miroslav. Optical trapping of nanoparticles and microparticles by a Gaussian standing wave. *Opt. Lett.* 1999, **24**(21), 1448–1450.

59. ZEMÁNEK, Pavel; JONÁŠ, Alexandr; LIŠKA, Miroslav. Simplified description of optical forces acting on a nanoparticle in the Gaussian standing wave. *J. Opt. Soc. Am. A*. 2002, **19**(5), 1025–1034.

60. ČIŽMÁR, T.; ŠILER, M.; ZEMÁNEK, P. An optical nanotrap array movable over a milimetre range. *Applied Physics B*. 2006, **84**(1), 197–203.

61. ŠILER, M.; ČIŽMÁR, T.; ŠERÝ, M.; ZEMÁNEK, P. Optical forces generated by evanescent standing waves and their usage for sub-micron particle delivery. *Appl. Phys. B*. 2006, **84**, 157–165.

62. ŠILER, Martin; ČIŽMÁR, Tomáš; JONÁŠ, Alexandr; ZEMÁNEK, Pavel. Surface delivery of a single nanoparticle under moving evanescent standing-wave illumination. *New. J. Phys.* 2008, **10**, 113010:1–16.

63. PRALLE, A.; PRUMMER, M.; FLORIN, E.L.; STELZER, E.H.K.; HÖRBER, J.K.H. Three-dimensional high-resolution particle tracking for optical tweezers by forward scattered light. *Microsc. Res. Tech.* 1999, **44**(5), 378–386.

64. GITTES, Frederick; SCHMIDT, Christoph F. Interference model for back-focal-plane displacement detection in optical tweezers. *Opt. Lett.* 1998, **23**(1), 7–9.

65. ROHRBACH, Alexander; STELZER, Ernst H. K. Three-dimensional position detection of optically trapped dielectric particles. *Journal of Applied Physics.* 2002, **91**(8), 5474–5488.

66. TAY, Jian Wei; HSU, Magnus T. L.; BOWEN, Warwick P. Quantum limited particle sensing in optical tweezers. *Phys. Rev. A.* 2009, **80**, 063806.

67. TOLIĆ-NØRRELYKKE, Simon F; SCHÄFFER, Erik; HOWARD, Jonathon; PAVONE, Francesco S; JÜLICHER, Frank; FLYVBJERG, Henrik. Calibration of optical tweezers with positional detection in the back focal plane. *Rev. Sci. Instrum.* 2006, **77**(10), 103101.

68. HEBESTREIT, Erik; FRIMMER, Martin; REIMANN Renéand Dellago, Christoph; RICCI, Francesco; NOVOTNY, Lukas. Calibration and energy measurement of optically levitated nanoparticle sensors. *Review of Scientific Instruments.* 2018, **89**(3), 033111.

69. CHEONG, Fook Chiong; KRISHNATREYA, Bhaskar Jyoti; GRIER, David G. Strategies for three-dimensional particle tracking with holographic video microscopy. *Opt. Express.* 2010, **18**(13), 13563–13573.

70. LEE, Sang-Hyuk; GRIER, David G. Holographic microscopy of holographically trapped three-dimensional structures. *Opt. Express.* 2007, **15**(4), 1505–1512.

71. KRISHNATREYA, Bhaskar Jyoti; COLEN-LANDY, Arielle; HASEBE, Paige; BELL, Breanna A.; JONES, Jasmine R.; SUNDA-MEYA, Anderson; GRIER, David G. Measuring Boltzmann's constant through holographic video microscopy of a single colloidal sphere. *American Journal of Physics.* 2014, **82**(1), 23–31.

72. MOYSES, Henrique W.; KRISHNATREYA, Bhaskar J.; GRIER, David G. Robustness of Lorenz-Mie microscopy against defects in illumination. *Opt. Express.* 2013, **21**(5), 5968–5973.

73. FORTES, F.J.; LASERNA, J.J. Characteristics of solid aerosols produced by optical catapulting studied by laser-induced breakdown spectroscopy. *Applied Surface Science.* 2010, **256**(20), 5924 –5928.

74. KONONENKO, T. V.; ALLONCLE, P.; KONOV, V. I.; SENTIS, M. Laser transfer of diamond nanopowder induced by metal film blistering. *Applied Physics A*. 2009, **94**(3), 531–536.

75. DOW, Alex R.; WITTRIG, Ashley M.; KENTTÄMAA, Hilkka I. Laser-Induced Acoustic Desorption Mass Spectrometry. *European Journal of Mass Spectrometry*. 2012, **18**(2), 77–92.

76. BEKSHAEV, Aleksandr; BLIOKH, Konstantin Y.; SOSKIN, Marat. Internal flows and energy circulation in light beams. *J. Opt.* 2011, **13**(5), 053001.

77. BERRY, M. V. Optical currents. *J. Opt. A*. 2009, **11**(9), 094001.

78. BLIOKH, Konstantin Y.; BEKSHAEV, Aleksandr Y.; NORI, Franco. Extraordinary momentum and spin in evanescent waves. *Nat. Commun.* 2014, **5**, 3300.

79. NEUGEBAUER, Martin; BAUER, Thomas; AIELLO, Andrea; BANZER, Peter. Measuring the Transverse Spin Density of Light. *Phys. Rev. Lett.* 2015, **114**(6). ISSN 0031-9007.

80. PFEIFER, Robert N. C.; NIEMINEN, Timo A.; HECKENBERG, Norman R.; RUBINSZTEIN-DUNLOP, Halina. Colloquium: Momentum of an electromagnetic wave in dielectric media. *Rev. Mod. Phys.* 2007, **79**(1), 1197–2016. ISSN 0034-6861. Available from DOI: 10.1103/RevModPhys.81.443.

81. ANTOGNOZZI, M.; BERMINGHAM, C. R.; HARNIMAN, R. L.; SIMPSON, S.; SENIOR, J.; HAYWARD, R.; HOERBER, H.; DENNIS, M. R.; BEKSHAEV, A. Y.; BLIOKH, K. Y.; NORI, F. Direct measurements of the extraordinary optical momentum and transverse spin-dependent force using a nano-cantilever. *Nat. Phys.* 2016, **12**(8), 731–735.

82. LIU, Lulu; DI DONATO, Andrea; GINIS, Vincent; KHEIFETS, Simon; AMIRZHAN, Arman; CAPASSO, Federico. Three-Dimensional Measurement of the Helicity-Dependent Forces on a Mie Particle. *Phys. Rev. Lett.* 2018, **120**(22), 223901.

83. ANGELSKY, O. V.; BEKSHAEV, A. Ya; MAKSIMYAK, P. P.; MAKSIMYAK, A. P.; HANSON, S. G.; ZENKOVA, C. Yu. Orbital rotation without orbital angular momentum: mechanical action of the spin part of the internal energy flow in light beams. *Opt. Express*. 2012, **20**(4), 3563–3571.

84. RUFFNER, David B.; GRIER, David G. Optical Forces and Torques in Nonuniform Beams of Light. *Phys. Rev. Lett.* 2012, **108**(17), 173602.

85. SUKHOV, Sergey; KAJORNDEJNUKUL, Veerachart; NARAGHI, Roxana Rezvani; DOGARIU, Aristide. Dynamic consequences of optical spin-orbit interaction. *Nat. Photon.* 2015, **9**(12), 809–812. ISSN 1749-4885. Available from DOI: 10.1038/NPHOTON.2015.200.

86. RODRIGUEZ-FORTUNO, Francisco J.; ENGHETA, Nader; MARTINEZ, Alejandro; ZAYATS, Anatoly V. Lateral forces on circularly polarizable particles near a surface. *Nat. Commun.* 2015, **6**. ISSN 2041-1723. Available from DOI: 10.1038/ncomms9799.

87. WANG, S. B.; CHAN, C. T. Lateral optical force on chiral particles near a surface. *Nat. Commun.* 2014, **5**. ISSN 2041-1723. Available from DOI: 10.1038/ncomms4307.

88. MAGALLANES, H.; BRASSELET, E. Macroscopic direct observation of optical spin-dependent lateral forces and left-handed torques. *ArXiv e-prints*. 2018. Available from arXiv: 1802.00607 [physics.optics].

89. DIVITT, Shawn; RONDIN, Loic; NOVOTNY, Lukas. Cancellation of nonconservative scattering forces in optical traps by counter-propagating beams. *Opt. Lett.* 2015, **40**(9), 1900–1903. ISSN 0146-9592. Available from DOI: 10.1364/OL.40.001900.

90. NIEMINEN, Timo A.; STILGOE, Alexander B.; HECKENBERG, Norman R.; RUBINSZTEIN-DUNLOP, Halina. Angular momentum of a strongly focused Gaussian beam. *J. Opt. A.* 2008, **10**(11), 115005. ISSN 1464-4258. Available from DOI: 10.1088/1464-4258/10/11/115005.

91. SVAK, V.; BRZOBOHATÝ, O.; SILER, M.; JÁKL, P.; KANKA, J.; ZEMÁNEK, P.; SIMPSON, S. H. Transverse spin forces and non-equilibrium particle dynamics in a circularly polarized vacuum optical trap. *Nature Communications*. 2018, **9**(1), 5453.

92. SIMPSON, Stephen H.; HANNA, Simon. First-order nonconservative motion of optically trapped nonspherical particles. *Phys. Rev. E.* 2010, **82**(3, 1), 031141. ISSN 1539-3755. Available from DOI: 10.1103/PhysRevE.82.031141.

93. IRRERA, Alessia; MAGAZZU, Alessandro; ARTONI, Pietro; SIMPSON, Stephen H.; HANNA, Simon; JONES, Philip H.; PRIOLO, Francesco; GUCCIARDI, Pietro Giuseppe; MARAGO, Onofrio M. Photonic Torque Microscopy of the Nonconservative Force Field for Optically Trapped Silicon Nanowires. *Nano Lett.* 2016, **16**(7), 4181–4188. ISSN 1530-6984. Available from DOI: 10.1021/acs.nanolett.6b01059.

94. BERRY, M. V.; SHUKLA, Pragya. Physical curl forces: Dipole dynamics near optical vortices. *J. Phys. A.* 2013, **46**(42), 422001.

95. BERRY, M. V.; SHUKLA, Pragya. Curl force dynamics: Symmetries, chaos and constants of motion. *New J. Phys.* 2016, **18**, 063018. ISSN 1367-2630.

96. THIRUNAMACHANDRAN, T. Intermolecular interactions in the presence of an intense radiation field. *Molecular Physics*. 1980, **40**, 393–399.

97. BURNS, M. M.; FOURNIER, J.-M.; GOLOVCHENKO, J. A. Optical Binding. *Phys. Rev. Lett.* 1989, **63**, 1233–1236.

98. TATARKOVA, S. A.; CARRUTHERS, A. E.; DHOLAKIA, K. One-Dimensional Optically Bound Arrays of Microscopic Particles. *Phys. Rev. Lett.* 2002, **89**, 283901.

99. SINGER, W.; FRICK, M.; BERNET, S.; RITSCH-MARTE, M. Self-organized array of regularly spaced microbeads in a fiber-optical trap. *J. Opt. Soc. Am. B*. 2003, **20**, 1568–1574.

100. KARÁSEK, V; ČIŽMÁR, T; BRZOBOHATỲ, O; ZEMÁNEK, P; GARCÉS-CHÁVEZ, V; DHOLAKIA, K. Long-range one-dimensional longitudinal optical binding. *Physical review letters*. 2008, **101**(14), 143601.

101. SIMPSON, Stephen H; ZEMÁNEK, Pavel; MARAGÒ, Onofrio M; JONES, Philip H; HANNA, Simon. Optical binding of nanowires. *Nano letters*. 2017, **17**(6), 3485–3492.

102. ARITA, Yoshihiko; WRIGHT, Ewan M.; DHOLAKIA, Kishan. Optical binding of two cooled micro-gyroscopes levitated in vacuum. *Optica*. 2018, **5**(8), 910–917.

103. BYKOV, Dmitry S.; XIE, Shangran; ZELTNER, Richard; MACHNEV, Andrey; WONG, Gordon K. L.; EUSER, Tijmen G.; RUSSELL, Philip St J. Long-range optical trapping and binding of microparticles in hollow-core photonic crystal fibre. *Light: Science & Applications*. 2018, **7**(1), 22.

104. ČIŽMÁR, T.; BRZOBOHATÝ, O.; DHOLAKIA, K.; ZEMÁNEK, P. The holographic optical micro-manipulation system based on counter-propagating beams. *Laser Phys. Lett.* 2011, **8**(1), 50–56.

105. DHOLAKIA, K.; ZEMÁNEK, P. Gripped by light: Optical binding. *Rev. Mod. Phys.* 2010, **82**, 1767–1791.

106. BRZOBOHATÝ, Oto; CHVÁTAL, Lukáš; ZEMÁNEK, Pavel. Optomechanical properties of optically self-arranged colloidal waveguides. *Opt. Lett.* 2019, **4**(3), 707–710.

107. LEITE, Ivo T.; TURTAEV, Sergey; JIANG, Xin; ŠILER, Martin; CUSCHIERI, Alfred; RUSSELL, Philip St. J.; ČIŽMÁR. Three-dimensional holographic optical manipulation through a high-numerical-aperture soft-glass multimode fibre. *Nature Photon.* 2018, **12**, 33–39.

108. SLEZAK, Bradley R.; D'URSO, Brian. A microsphere molecule: The interaction of two charged microspheres in a magneto-gravitational trap. *Appl. Phys. Lett.* 2019, **114**(24), 244102.

109. SVAK, Vojtěch; FLAJŠMANOVÁ, Jana; CHVÁTAL, Lukáš; ŠILER, Martin; JONÁŠ, Alexandr; JEŽEK, Jan; SIMPSON, Stephen H.; ZEMÁNEK, Pavel; BRZOBOHATÝ, Oto. Stochastic dynamics of optically bound matter levitated in vacuum. *Optica.* 2021, **8**(2), 220–229.

110. MACKOWSKI, Daniel. The Extension of Mie Theory to Multiple Spheres. In: *Mie Theory Basics Appl.* Ed. by HERGERT, Wolfram; WRIEDT, Thomas. Berlin, Heidelberg: Springer Berlin Heidelberg, 2012, pp. 223–256. ISBN 978-3-642-28738-1. Available from DOI: 10.1007/978-3-642-28738-1_8.

111. KARÁSEK, V.; ČIŽMÁR, T.; BRZOBOHATÝ, O.; ZEMÁNEK, P.; GARCÉS-CHÁVEZ, V.; DHOLAKIA, K. Long-range one-dimensional longitudinal optical binding. *Phys. Rev. Lett.* 2008, **101**(14), 143601. ISSN 0031-9007. Available from DOI: 10.1103/PhysRevLett.101.143601.

112. BRZOBOHATÝ, O.; KARÁSEK, V.; ČIŽMÁR, T.; ZEMÁNEK, P. Dynamic size tuning of multidimensional optically bound matter. *Appl. Phys. Lett.* 2011, **99**(10), 101105. ISSN 00036951. Available from DOI: 10.1063/1.3634007.

113. NGUYENA, HC; BERNARDS, Fabian. Entanglement dynamics of two mesoscopic objects with gravitational interaction. *Eur. Phys. J. D.* 2020, **74**(69).

114. QVARFORT, Sofia; BOSE, Sougato; SERAFINI, Alessio. Mesoscopic entanglement through central-potential interactions. *J. Phys. B: At. Mol. Opt. Phys.* 2020, **in press**. Available from eprint: 1812.09776.

115. FORD, Joseph. The Fermi-Pasta-Ulam problem: Paradox turns discovery. *Phys. Rep.* 1992, **213**(5), 271–310.

116. LIVI, Roberto; PETTINI, Marco; RUFFO, Stefano; SPARPAGLIONE, Massimo; VULPIANI, Angelo. Equipartition threshold in nonlinear large Hamiltonian systems: The Fermi-Pasta-Ulam model. *Phys. Rev. A.* 1985, **31**(2), 1039–1045.

117. GIESELER, Jan; DEUTSCH, Bradley; QUIDANT, Romain; NOVOTNY, Lukas. Subkelvin Parametric Feedback Cooling of a Laser-Trapped Nanoparticle. *Phys. Rev. Lett.* 2012, **109**.

118. LI, T.; KHEIFETS, S.; RAIZEN, M. G. Millikelvin cooling of an optically trapped microsphere in vacuum. *Nature Phys.* 2011, **7**, 527–530.

119. JONES, Philip H.; MARAGÒ, Onofrio M.; VOLPE, Giovanni. *Optical Tweezers: Principles and Applications*. Cambridge University Press, 2015.

120. SINGH, Rajesh; GHOSH, Dipanjan; ADHIKARI, R. Fast Bayesian inference of the multivariate Ornstein-Uhlenbeck process. *Phys. Rev. E.* 2018, **98**, 012136.

121. RICHLY, Maximilian; TÜRKCAN, Silvan; LE GALL, Antoine; FISZMAN, Nicolas; MASSON, jean-baptiste; WESTBROOK, Nathalie; PERRONET, Karen; ALEXANDROU, Antigoni. Calibrating optical tweezers with Bayesian inference. *Optics express*. 2013, **21**, 31578–90.

122. EL BEHEIRY, Mohamed; TÜRKCAN, Silvan; RICHLY, Maximilian; ANTOINE, Triller; ALEXANDROU, Antigoni; DAHAN, Maxime; MASSON, jean-baptiste. A Primer on the Bayesian Approach to High-Density Single-Molecule Trajectories Analysis. *Biophysical Journal*. 2016, **110**, 1209–1215.

123. BERA, Sudipta; PAUL, Shuvojit; SINGH, Rajesh; GHOSH, Dipanjan; KUNDU, Avijit; BANERJEE, Ayan; ADHIKARI, Ronojoy. Fast Bayesian inference of optical trap stiffness and particle diffusion. *Scientific Reports*. 2017, **7**, 41638.

124. PÉREZ GARCÍA, Laura; DONLUCAS PÉREZ, Jaime; VOLPE, Giorgio; V. ARZOLA, Alejandro; VOLPE, Giovanni. High-performance reconstruction of microscopic force fields from Brownian trajectories. *Nature Communications*. 2018, **9**(1), 5166.

125. WU, Pinyu; HUANG, Rongxin; TISCHER, Christian; JONAS, Alexandr; FLORIN, Ernst-Ludwig. Direct Measurement of the Nonconservative Force Field Generated by Optical Tweezers. *Phys. Rev. Lett.* 2009, **103**, 108101.

126. VOLPE, Giovanni; HELDEN, Laurent; BRETTSCHNEIDER, Thomas; WEHR, Jan; BECHINGER, Clemens. Influence of Noise on Force Measurements. *Phys. Rev. Lett.* 2010, **104**, 170602.

127. BRETTSCHNEIDER, Thomas; VOLPE, Giovanni; HELDEN, Laurent; WEHR, Jan; BECHINGER, Clemens. Force measurement in the presence of Brownian noise: Equilibrium-distribution method versus drift method. *Phys. Rev. E.* 2011, **83**, 041113.

128. GIESELER, Jan; GOMEZ-SOLANO, Juan Ruben; MAGAZZÙ, Alessandro; CASTILLO, Isaac Pérez; GARCÍA, Laura Pérez; GIRONELLA-TORRENT, Marta; VIADER-GODOY, Xavier; RITORT, Felix; PESCE, Giuseppe; ARZOLA, Alejandro V.; VOLKE-SEPULVEDA, Karen; VOLPE, Giovanni. *Optical Tweezers: A Comprehensive Tutorial from Calibration to Applications*. 2020. Available from arXiv: `2004.05246 [physics.optics]`.

129. PARK, Haesung; LEBRUN, Thomas W. Parametric Force Analysis for Measurement of Arbitrary Optical Forces on Particles Trapped in Air or Vacuum. *ACS Photonics*. 2015, **2**(10), 1451–1459.

130. RICCI, F.; CUAIRAN, M. T.; CONANGLA, G. P.; SCHELL, A. W.; QUIDANT, R. Accurate Mass Measurement of a Levitated Nanomechanical Resonator for Precision Force-Sensing. *Nano Letters*. 2019, **19**(10).

131. BERG-SØRENSEN, K.; FLYVBJERG, H. Power spectrum analysis for optical tweezers. *Rev. Sci. Instrum.* 2004, **75**, 594–612.